INTERIM REPORT NO. 2

On Research Grant No. NsG 221-62

NATIONAL AERONAUTICS AND SPACE ADMINISTRATION

A LOG PERIODIC MONOPOLE ANTENNA IN A DIELECTRIC FILLED CAVITY

by

Richard L. Whale
Clayton Clark

June 30, 1963

ANTENNAS AND PROPAGATION LABORATORY
Department of Electrical Engineering
Engineering Experiment Station
UTAH STATE UNIVERSITY

A LOG PERIODIC MONOPOLE ANTENNA
IN A DIELECTRIC FILLED CAVITY

by

Richard L. Whale
Clayton Clark

June 30, 1963

ANTENNAS AND PROPAGATION LABORATORY
Department of Electrical Engineering
Engineering Experiment Station
UTAH STATE UNIVERSITY

ACKNOWLEDGMENTS

TABLE OF CONTENTS

LIST OF TABLES

LIST OF FIGURES

Figure   Page

INTRODUCTION

This report covers the investigation of the input impedance char-
acteristics and the radiation patterns of a log-periodic monopole
antenna when flush mounted in a dielectric filled cavity. The work
has four objectives:

    (1) To illustrate basic design considerations of a log-periodic
monopole antenna for use in a dielectric medium,

    (2) To show that the driving point impedance characteristics
of the antenna repeat periodically with frequency when the
antenna is submerged in a dielectric filled cavity,

    (3) To show that the radiation pattern is essentially independent
of frequency,

    (4) To provide preliminary information necessary for the
detailed analysis of a log-periodic antenna when flush-mounted
in a dielectric filled cavity.

The basic log-periodic structure employed in this study was the
log-periodic monopole antenna (see Figure 1a). The H-plane radiation
field equation for a log-periodic monopole antenna over an air filled
cavity was derived. An approximate solution of this equation was made.
The main lobe direction and shape was predicted for the air filled
cavity. This lobe pattern was compared with air cavity pattern
measurements.

Radiation pattern and impedance measurements were made on the air cavity model and on models in which relative dielectric constants were 2.25 and 4.00. The measurements were made at frequencies between 2.0 Gc and 4.0 Gc. The equation for the dielectric filled cavity was set up but solution of the equation is possible only by computer methods. Work is progressing on programming the radiation equations for the IBM 1620 computer. Comparisons between predictions and measurements for dielectric filled cavities will be the subject of a future report.
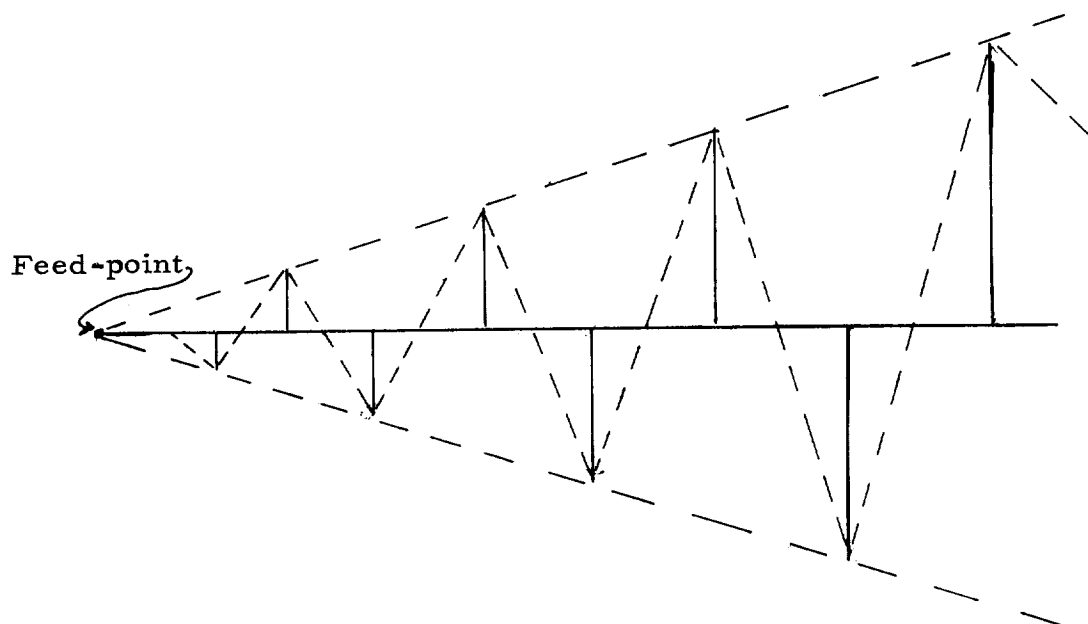
Figure 1a. Log-periodic monopole antenna. This antenna (solid
lines) is an approximation of the triangular-tooth structure (dashed
lines).
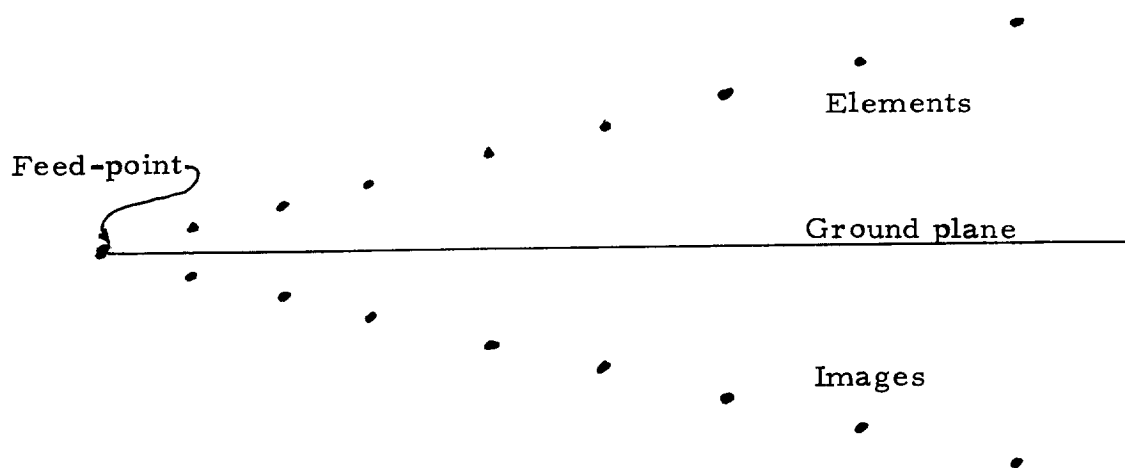
Figure 1b. Mounted log-periodic monopole antenna.

HISTORY

Antennas having unusually wide frequency bandwidths were first mentioned in the literature by DuHamel and Isbell (1957). Their paper described a structure which was called a log-periodic antenna because its radiation and impedance characteristics repeated periodically with the logarithm of frequency. Since 1957 several papers have been presented describing various studies of different types of log-periodic structures, for example: DuHamel and Ore (1958), and Dyson (1962).

The first log-periodic antennas had solid teeth. DuHamel and Ore (1959) studied planar and non-planar triangular-tooth antennas, trapezoidial-tooth structures, and non-planar triangular-tooth structures. Some of these antennas consisted of wire outlines for the teeth and were found to perform almost as well as the solid tooth antennas.

In 1960, Bell, Elfving, and Franks made near-field measurements of a triangular-tooth log-periodic antenna. These measurements suggested that each tooth could be approximated as a single thin linear element. The structure resulting from this approximation, and utilized in this study, is shown in Figure 1a. This unit is mounted above and at an angle to a reflecting sheet as shown in Figure 1b. It is referred to as a log-periodic monopole antenna.

This antenna is equivalent to one half of the log-periodic dipole array investigated by Isbell (1960).

Brownell (1961) studied the log-periodic monopole antenna placed over a ground plane and verified that the structure still maintained its log-periodic characteristics for various angles of the antenna with respect to this ground plane. Brownell also suggested that this antenna be investigated for use in a cavity. The results of this study were reported by Clark, Jones, and Leigh (1962).

The work on the log-periodic monopole antenna mounted over a dielectric filled cavity was begun in 1961 after a suggestion of Fred P. Brownell.

THEORY

Log-Periodic Monopole Antenna Design for Dielectric Mediums

Design procedure for various log-periodic antennas is available in the literature: Clark, Jones, and Leigh (1962), Brownell (1961), and Carrel (1961), Elfving (1961), and others. One of these design procedures is briefly reviewed here because it has been used in the design and analysis of the log-periodic monopole antenna.

It is desired, with the log-periodic antenna, to have the driving point impedance and radiation patterns essentially independent of frequency. This requires the lengths of the elements to be varied such that at least one of the elements will be near resonance for any desired frequency of operation and that the spacing between elements be such that elements near the resonant element may contribute to the radiation pattern, thus some gain will be realized. Furthermore, the transition of electrical characteristics must be smooth as the radiating segment of elements (active region) shifts along the antenna with changing frequency.

Certain design parameters, characteristic lengths and angles must be defined for the design and analysis of the antenna; these parameters are shown in Figure 2. The taper angle α is defined as

$$\alpha = \tan^{-1} \frac{\lambda_n}{S_n} \tag{1}$$

The logarithmic ratio parameter τ is defined, for purposes of this report, as

$$\tau = \frac{\ell_{n-1}}{\ell_n} = \frac{S_{n-1}}{S_n} \tag{2}$$

where ℓ_n and S_n are defined as shown in Figure 2, and n is the number of a general tooth.
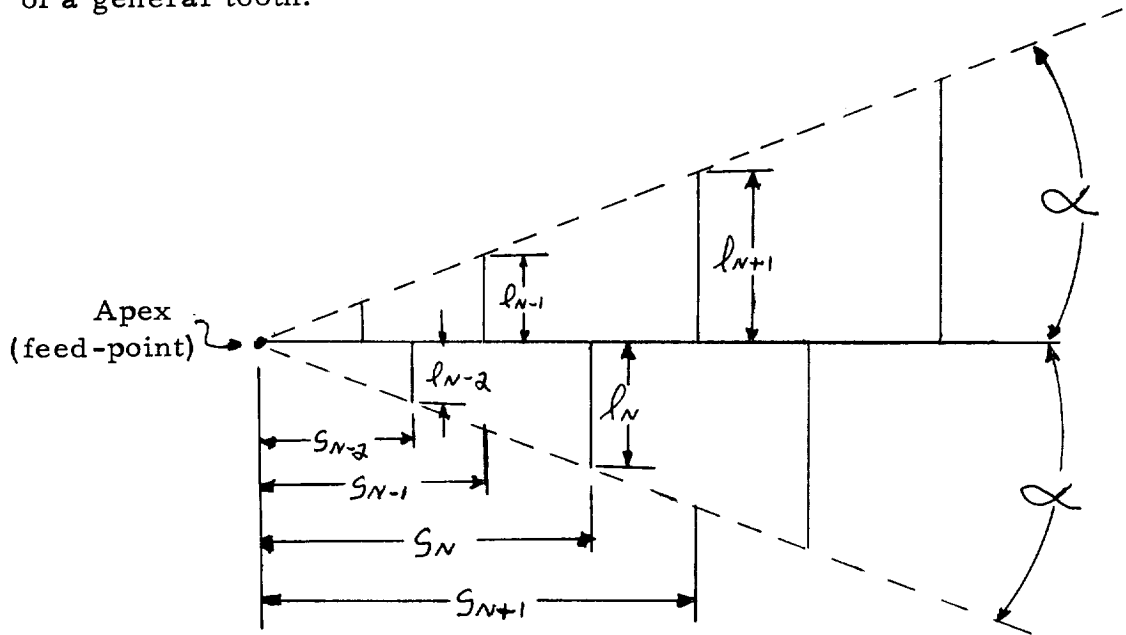
Figure 2. Characteristic dimensions of a log-periodic monopole antenna.

The third specification necessary for the antenna design is the desired frequencies of operation. Thus the log-periodic antenna can be designed, theoretically, to operate at any range of frequencies desired. The upper cutoff frequency f_h is determined by the length of the shortest element of the array (or by other stray effects) while the lower cutoff frequency f_1 is controlled by the length of the longest element.

As shown in equation (2) the lengths and spacings of the elements are related by the ratio τ. The length of the elements of order n are given by $\tau^n L$ where L is the length of the longest element. The spacings of elements of order n from the apex are given by $\tau^n S$ where S is the length of the antenna (the distance from the apex to the longest element).

For this specific study a log-periodic monopole antenna was submerged in a dielectric filled cavity (see Figures 3a and 3b). In previous designs of log-periodic antennas τ and α were defined, as in equations (1) and (2), in terms of lengths. These definitions were adequate for free space conditions but are not for dielectric mediums.

A more basic understanding of τ and α is necessary for the design of antennas in dielectric mediums. The logarithmic ratio is actually an array factor, as discussed by Isbell (1960), which relates the radian phase distances between elements of the antenna. Therefore by redefining the lengths of Figure 2 in terms of wave lengths λ as

$$\ell_n = A \lambda_n \tag{3}$$

and
$$S_n = B \lambda_n \tag{4}$$

This redefines τ and α as

$$\tau = \frac{\ell_{n-1}}{\ell_n} = \frac{A\lambda_{n-1}}{A\lambda_n} = \frac{B\lambda_{n-1}}{B\lambda_n} = \frac{\lambda_{n-1}}{\lambda_n} \tag{5}$$

3 dimensional view showing antenna under the dielectric cover
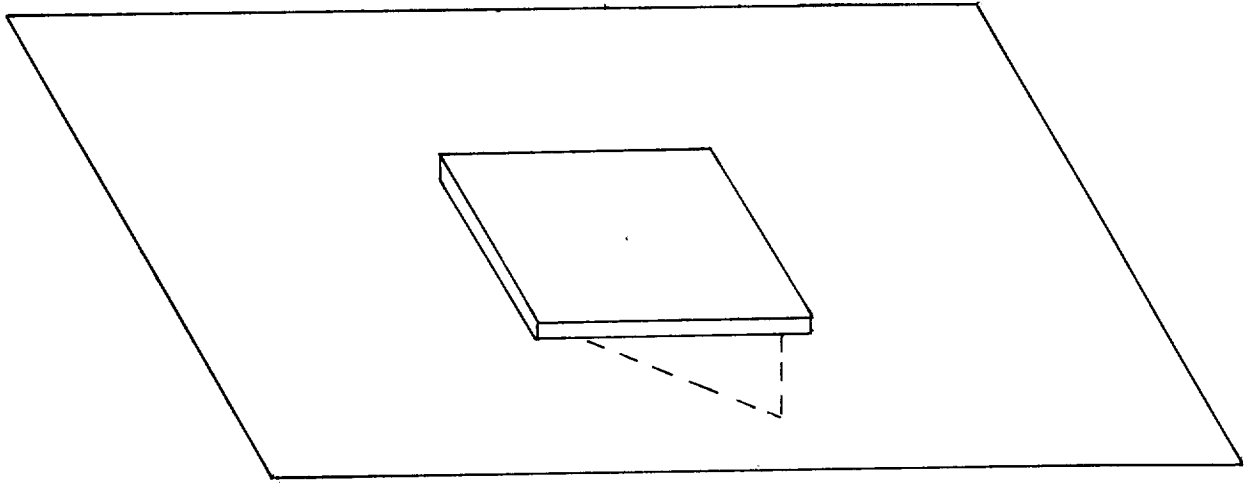
Figure 3a. Monopole-tooth antenna mounted flush. The antenna
is submerged in the dielectric by placing the dielectric cover over
the filled cavity.

3 dimensional view of antenna without the dielectric cover
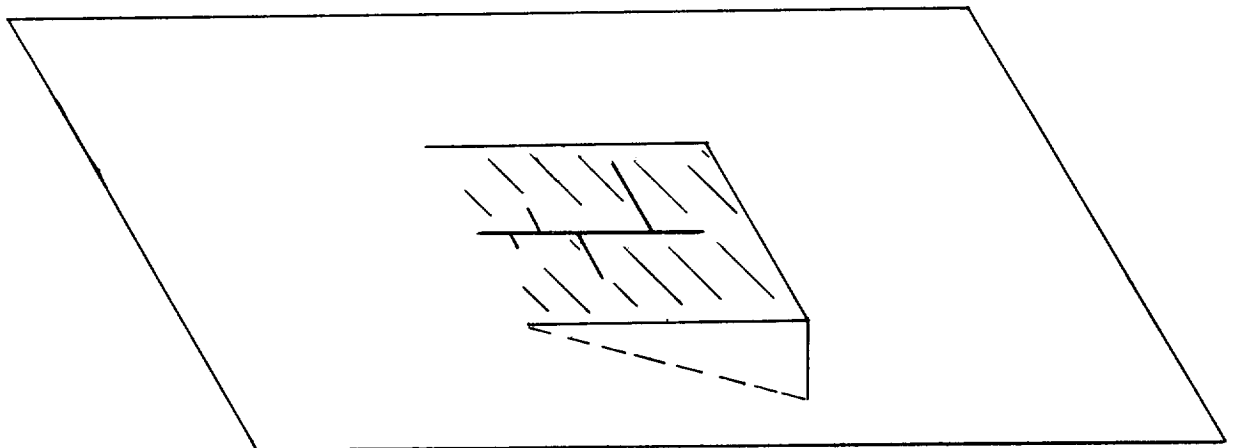
Figure 3b. Monopole-tooth antenna mounted flush. The antenna
is flush with the aperture of a dielectric filled cavity. Illustrated
without the dielectric cover.

and
$$a = \tan^{-1} \frac{B\lambda_n}{A\lambda_n} \qquad (6)$$

where λ_n is the wave length of the excitation frequency f_n,

A is the relative length of 1_n to the wave length λ_n,

B is the relative length of S_n to the wave length of λ_n.

It is therefore apparent that the presence of a dielectric makes no difference to the logarithmic ratio τ, but does alter the taper angle a.

Since λ_n can be expressed as a function of the dielectric medium,

$$\lambda_n' = \frac{\lambda_n}{\sqrt{\mu_r \epsilon_r}} \qquad (7)$$

where λ_n' is the wave length in the dielectric medium,

λ_n is the free space wave length,

equations (5) and (6) can be used to design antennas for dielectric mediums. The actual design of the antennas for the experimental part of this study is illustrated in the section on Experimentation.

Analysis of a Log-Periodic Monopole Antenna When Flush-Mounted Over a Cavity

Bell, Elfving, and Franks (1960) made near-field measurements of a triangular-tooth antenna. Their study showed that a wave originated at the apex (antenna feed point) and propagated on the structure toward the active region of the antenna. In the active region this wave decayed rapidly because it was launched as a radiated wave, thus, the wave on the structure had negligible amplitude beyond this

region. The active region of the antenna is that segment which produces the radiated wave. This region consists of elements that are near the resonant frequency and thus contribute the majority of the energy to the radiated wave.

The active region of the triangular-tooth antenna investigated by Bell, Elfving, and Franks (1960) consisted of five elements and centered approximately on the tooth nearest the resonant length. The number of elements in the active region is determined by the logarithmic ratio τ and the taper angle α. For a fixed value of α, more active elements are associated with a larger τ and fewer active elements are associated with a smaller τ.

Since the log-periodic monopole antenna is an unbalanced structure, it is fed against a ground plane. With such a structure, the analysis of the radiation pattern is accomplished by the "Method of Images." Figure 4 shows the active region of the antenna and its mirror image. The following derivation of the H-plane radiation equation assumes that four consecutive antenna elements constitute the active region for an antenna with the τ and α of this study. This assumption is based on an estimate of the element impedances, at the frequency of operation, which determine the elements that contribute the majority of the energy to the radiation pattern.

The logarithmic ratio τ as previously mentioned, is defined as

$$\tau = \frac{\ell_{n-1}}{\ell_n} = \frac{S_{n-1}}{S_n} \tag{2}$$
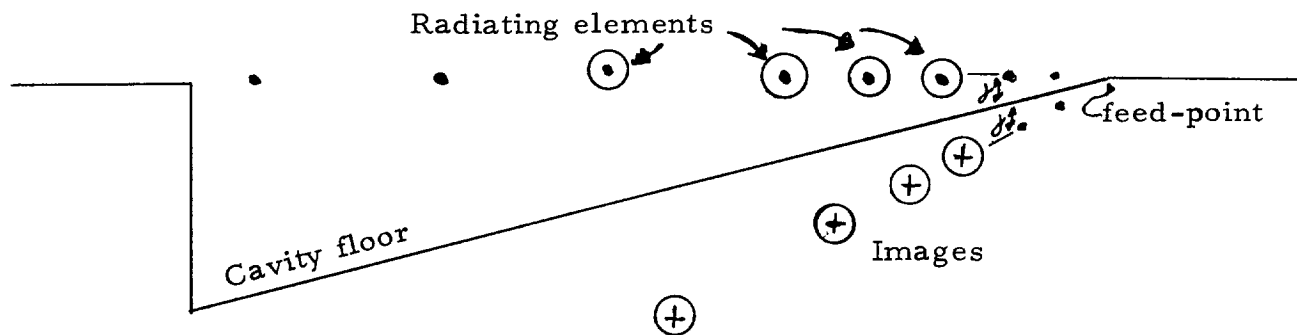
Figure 4. Log-periodic monopole antenna radiating elements. Shown is the side view of the antenna and its "mirror image."
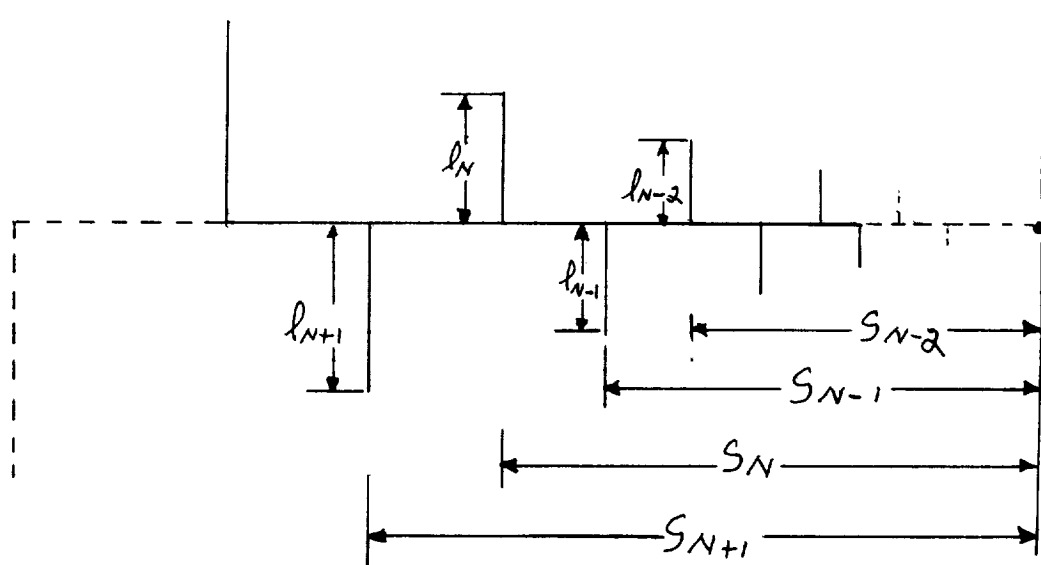
Figure 5. General dimensions of the log-periodic monopole antenna. Distances are from the "feed" point to the active region of the antenna.

Referring to Figure 5, if ℓ_n is the resonant element at frequency f_n then element ℓ_{n-1} resonates at frequency $f_{n-1} = f_n/\tau$. Element ℓ_{n-2} resonates at frequency $f_{n-2} = f_n/\tau^2$ and element ℓ_{n+1} resonates at frequency $f_{n+1} = \tau f_n$.

The particular log-periodic monopole antenna used in this study was designed so that the distance from the feed point of the antenna to the resonant element was one wave length at any frequency within the range of operation. Therefore,

$$S_n = \lambda_n = C/f_n$$

where λ_n is the wave length of the resonant frequency,

C is the velocity of light in free space.

Similar expressions may be written for the other distances in the active region, in terms of τ and the excitation frequency f_n:

$$S_{n+1} = \lambda_{n+1} = \frac{C}{f_{n+1}} = \frac{C}{\tau f_n} \tag{8}$$

$$S_{n-1} = \lambda_{n-1} = \frac{C}{f_{n-1}} = \frac{\tau C}{f_n} \tag{9}$$

$$S_{n-2} = \lambda_{n-2} = \frac{C}{f_{n-2}} = \frac{\tau^2 C}{f_n} \tag{10}$$

The phase shift in radians, dr, as the wave travels between elements ℓ_{n+1} and ℓ_n is

$$\frac{2\pi}{\lambda_n} (S_{n+1} - S_n) = 2\pi \left(\frac{1}{\tau} - 1\right) \tag{11}$$

radians. The corresponding phase shifts for other active elements and their "mirror" can be expressed as shown in Figure 6. If the antenna is mounted over a cavity in a large conducting sheet the cavity floor becomes the ground plane, as shown in Figure 7.

$dr + 2\pi \left(\frac{1}{\tau} - 1\right) \sin \gamma$

dr

$dr - [2\pi(1-\tau) \sin \gamma]$

$dr - [2\pi(1-\tau^2) \sin \gamma]$
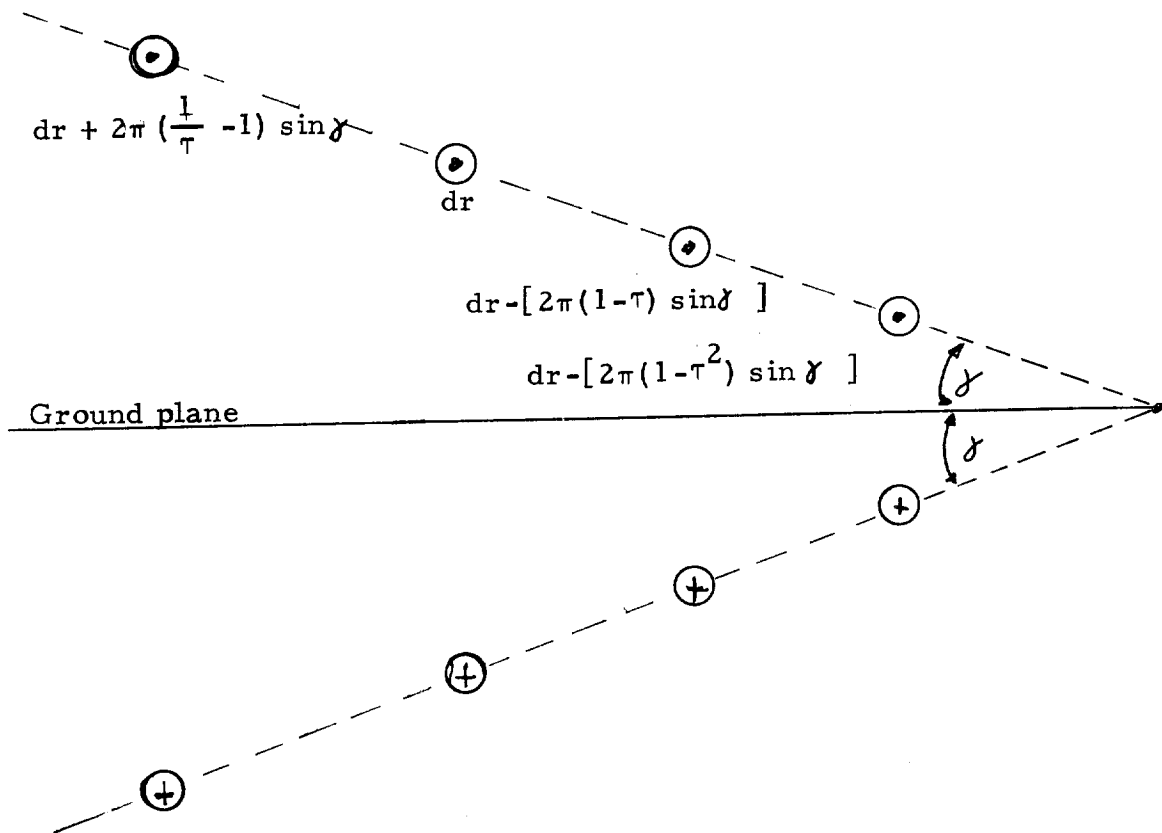
Ground plane

Figure 6. The phase shifts between the active elements and their images. The distance d_r is the perpendicular distance from the resonant element l_n to the ground plane. γ is the angle the antenna plane makes with the ground plane.

The cosine law is used to compute the relative distances which refer the phase shifts of the images to the element l_n. Figure 7 shows the definition of the following phase shifts.

Figure 7. Specification of distances between elements. The distances are in radians of phase shift from the active elements and images to the resonant element l_n.

$$dr_2 = 2\pi (1-\tau)$$

$$dr_1 = 2\pi \left(\frac{1}{\tau} -1\right)$$

$$dr_7 = 2[dr - 2\pi (1-\tau) \sin \gamma]$$

$$dr_0 = 2dr$$

$$dr_4 = 2[dr + 2\pi \left(\frac{1}{\tau} -1\right) \sin \gamma] \tag{14}$$

$$dr_5 = \left\{4[dr + 2\pi(\frac{1}{\tau} - 1) \sin \gamma]^2 + [2\pi (\frac{1}{\tau} - 1)]^2 \right.$$
$$\left. -4[dr + 2\pi(\frac{1}{\tau} - 1) \sin \gamma] \, 2\pi(\frac{1}{\tau} - 1) \cos (90^\circ - \gamma)\right\}^{\frac{1}{2}}$$

$$dr_{10} = dr_2 + dr_3 = 2\pi(1 - \tau^2)$$

$$dr_9 = 2[dr - 2\pi (1 - \tau^2) \sin \gamma]$$

$$dr_8 = \left\{4[dr - 2\pi(1 - \tau^2) \sin \gamma]^2 + [2\pi (1 - \tau^2)]^2 - 8\pi[dr - 2\pi(1 - \tau^2)\sin \gamma] \right.$$
$$\left. (1 - \tau^2) \cos (90^\circ + \gamma)\right\}^{\frac{1}{2}}$$

$$dr_6 = \left\{4[dr - 2\pi(1 - \tau) \sin \gamma]^2 + [2\pi(1 - \tau)]^2 \right.$$
$$\left. -8\pi(1 - \tau)[dr - 2\pi(1 - \tau)\sin \gamma] \cos(90^\circ + \gamma)\right\}^{\frac{1}{2}}$$

The radiation pattern is the summation of the contribution from all of the radiating elements and their mirror images. Referring to Figure 8, the radiation equation may be expressed as

$$E_T = E_{n-2} e^{j\psi_{n-2}} - E_{n-2} e^{j\psi'_{n-2}} + E_{n-1} e^{j\psi_{n-1}} - E_{n-1} e^{j\psi'_{n-1}} + E_n e^{j\psi_n}$$
$$- E_n e^{j\psi'_n} + E_{n+1} e^{-j\psi_{n+1}} - E_{n+1} e^{j\psi'_{n+1}} \qquad (15)$$

where E_n is the magnitude of the electric field contributed by element ℓ_n.

The exponential function, ψ_n's are:
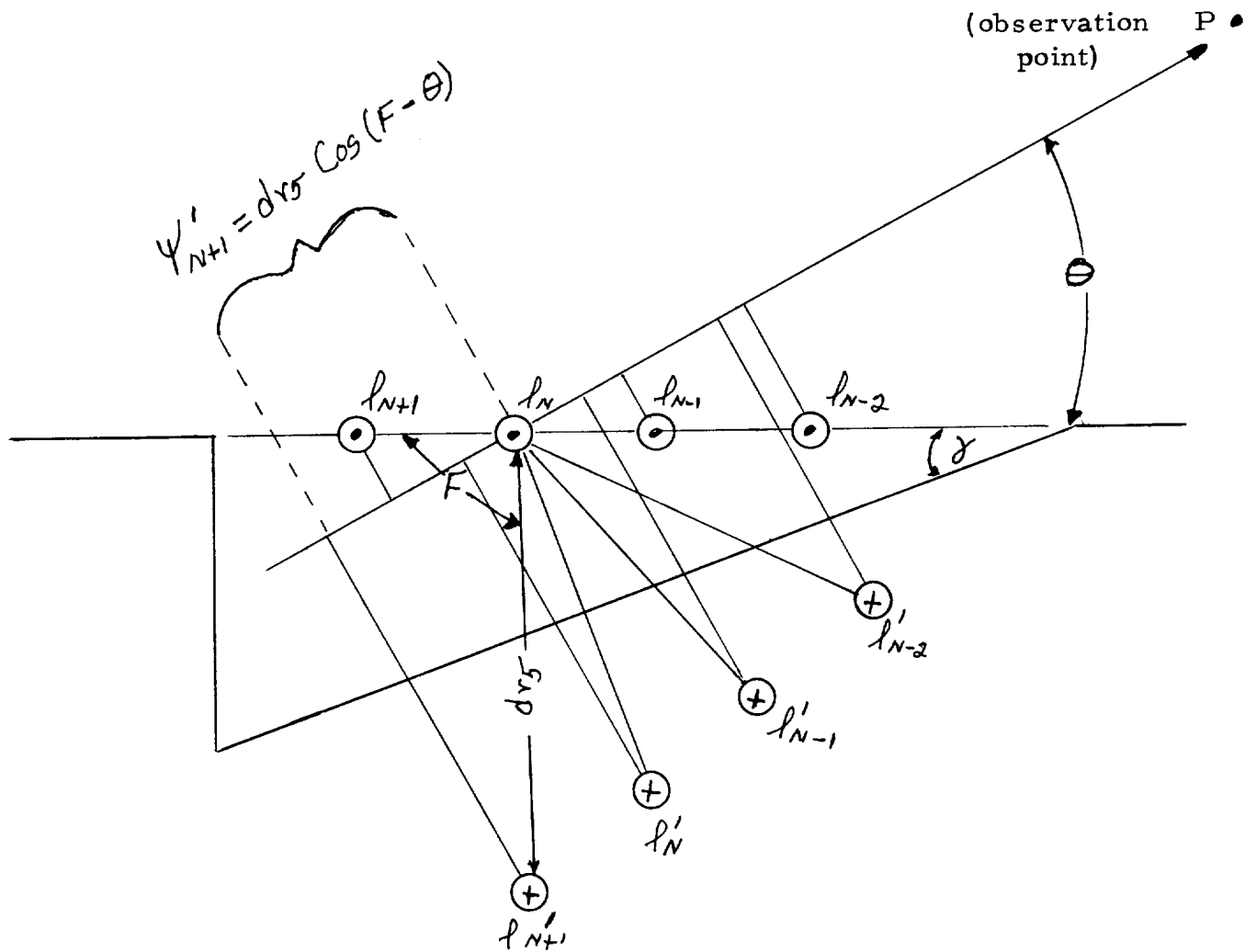
Figure 8. The relative phase shifts of the sources as a function of θ. The phase shifts are with respect to the reference point ℓ_n. These phase differences are calculated from the travel distances from each element or image to an observation point P.

$$\psi_{n-2} = dr_{10} \cos \theta$$

$$\psi'_{n-2} = dr_8 \cos (K + \theta)$$

$$\psi_{n-1} = dr_2 \cos \theta$$

$$\psi'_{n-1} = dr_6 \cos (C + \theta)$$

$$\psi_n = 0$$

$$\psi'_n = 2dr \cos (D + \theta)$$

$$\psi_{n+1} = dr_1 \cos \theta$$

$$\psi'_{n+1} = dr_5 \cos (F - \theta) \qquad (16)$$

where angles K, C, D, and F are expressed as:

$$K = \cos^{-1} \frac{(dr_{10})^2 + (dr_8)^2 - (dr_9)^2}{2 (dr_{10}) (dr_8)}$$

$$C = \cos^{-1} \frac{(dr_2)^2 + (dr_6)^2 - (dr_7)^2}{2 (dr_2) (dr_6)}$$

$$D = 90^\circ - \gamma \qquad (17)$$

$$F = \cos^{-1} \frac{(dr_1)^2 + (dr_5)^2 - (dr_4)^2}{2 (dr_1)(dr_5)}$$

For actual evaluation of E_T from equation (15), further informa-tion is necessary. A relation between the resistance of each monopole element and the contribution of these monopoles to the radiation field may be developed as follows:

$$E_n \text{ radiated} = k I_n = \frac{V_n}{Z_n} \qquad (18)$$

where E_n = the contribution to the field from the element 1_n

I_n = current at the base of element 1_n

V_n = voltage at base of element 1_n

Z_n = base impedance of 1_n

k = proportionality constant

Similar expressions may be stated for E_{n+1}, E_{n-1}, and E_{n-2}. By normalizing each of the expressions to E_n, the resulting expressions are:

$$\frac{E_n}{E_n} = 1$$

$$\frac{E_{n-1}}{E_n} = \frac{V_{n-1} \, Z_n}{V_n \, Z_{n-1}} = \frac{|V_{n-1}| \underline{/\delta_{n-1}} \, Z_n}{|V_n| \underline{/0} \, Z_{n-1}}$$

$$\frac{E_{n-2}}{E_n} = \frac{V_{n-2} \, Z_n}{V_n \, Z_{n-2}} = \frac{|V_{n-2}| \underline{/\delta_{n-2}} \, Z_n}{|V_n| \underline{/0} \, Z_{n+2}}$$

$$\frac{E_{n+1}}{E_n} = \frac{V_{n+1} \, Z_n}{V_n \, Z_{n+1}} = \frac{|V_{n+1}| \underline{/\delta_{n+1}} \, Z_n}{|V_n| \underline{/0} \, Z_{n+1}} \tag{19}$$

where δ_{n-2}, δ_{n-1}, δ_{n+1} are the voltage phases with respect to the voltage V_n.

The near-field measurements of Bell, Elfving, and Franks (1960) showed that two waves existed on the antenna; a transmission line wave which originated at the apex and propagated toward the active region, and a radiated wave which propagated away from the active region toward the apex. It seems proper, therefore, that each element of the antenna may be considered as a separate monopole antenna, and the center rod as a transmission line "feeding" the elements.

In this first order solution of the radiation pattern equation, mutual impedances have been neglected, except insofar as their effects may have been included in the estimate of the base impedance of each element. It was also assumed that the voltage wave, feeding the active region, remained constant in magnitude but variable in phase over this region. Thus, $|V_{n+1}| = |V_n| = |V_{n-1}| = |V_{n-2}|$ and thus

equations (19) can be expressed as:

$$\frac{E_n}{E_n} = 1$$

$$\frac{E_{n-1}}{E_n} = \frac{Z_n}{Z_{n-1}} \quad \frac{\delta_{n-1}}{0}$$

$$\frac{E_{n-2}}{E_n} = \frac{Z_n}{Z_{n-2}} \quad \frac{\delta_{n-2}}{0}$$

$$\frac{E_{n+1}}{E_n} = \frac{Z_n}{Z_{n+1}} \quad \frac{\delta_{n+1}}{0} \tag{20}$$

where Z_n is the base impedance of element 1_n,

Z_{n-1} is the base impedance of element 1_{n-1}

δ_{n-2} is the relative voltage phase of V_{n-2} with

respect to V_n.

Equation (15) can now be expressed, in normalized form, as

$$\frac{E_T}{E_n} = \frac{Z_n}{Z_n} (e^{j\psi_{n-2} + \delta_{n-2}} - e^{j\psi'_{n-2} + \delta_{n-2}})$$

$$+ \frac{Z_n}{Z_{n-1}} (e^{j\psi_{n-1} + \delta_{n-1}} - e^{j\psi'_{n-1} + \delta_{n-1}}) + e^{j\psi_n} - e^{j\psi'_n}$$

$$+ \frac{Z_n}{Z_{n+1}} (e^{-j(\psi_{n+1} + \delta_{n+1})} - e^{j\psi'_{n+1} + \delta_{n+1}}) \tag{21}$$
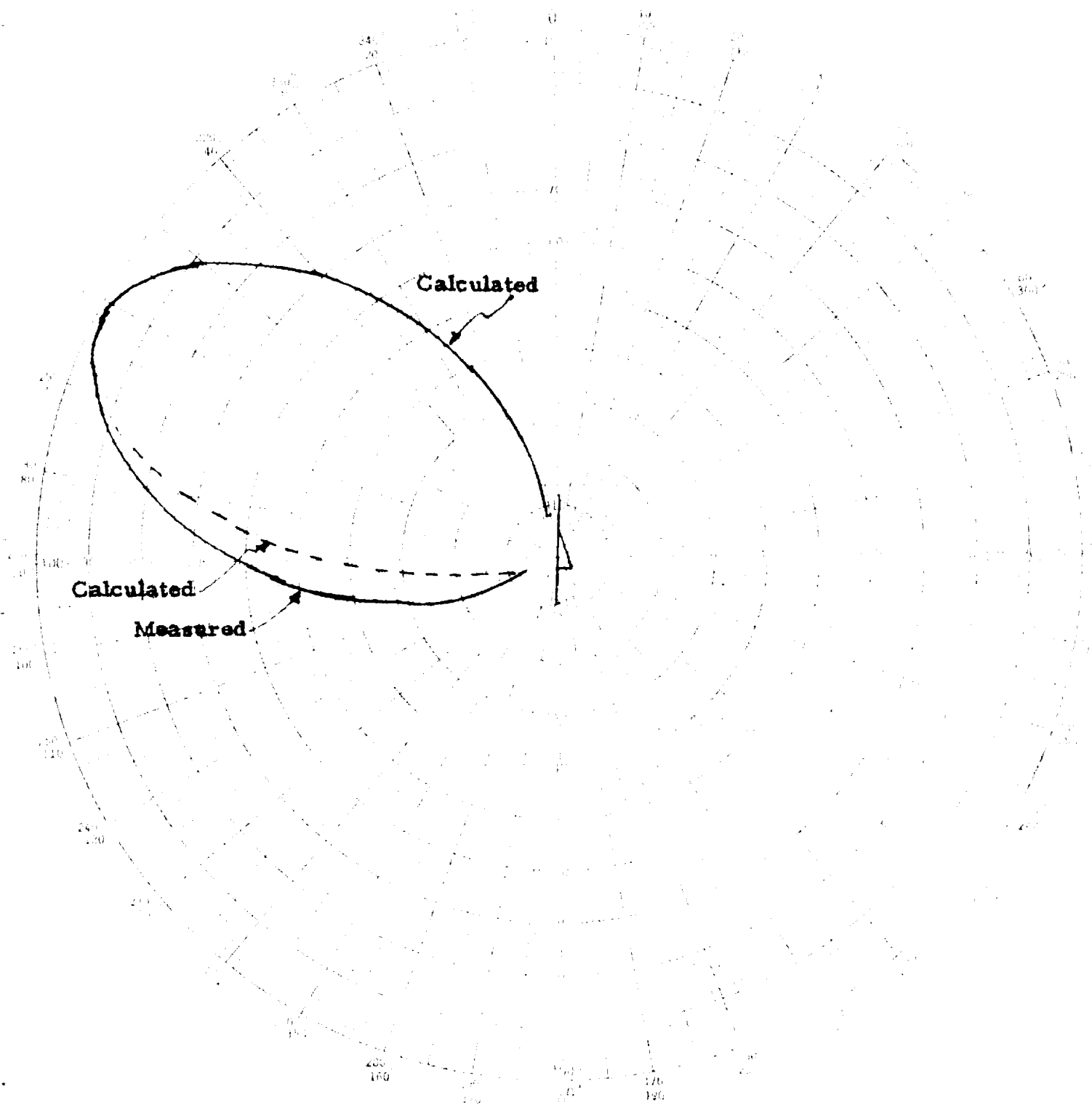
For actual calculations using equation (21), the values of

Figure 9. Comparison of measured to computed H-plane
pattern. Computations were made with following values:
$\tau = 0.85$, $a = 14^{\circ}$, $\gamma = 15^{\circ}$, $f = 1.8$ Gc.

Z_n, Z_{n+1}, etc., were estimated from the graphs on monopole

impedances in Schelkunoff and Friis (1952). The phase angles of

the voltages "feeding" the elements in the active region were deter-

mined on the basis that the transmission line wave propagated at

the speed of light through the active region. The results of these

calculations are illustrated in a comparison with the actual measured

radiation pattern as shown in Figure 9.

Basic Considerations for Analysis of the Log-periodic Monopole Antenna When Flush-Mounted over a Dielectric Filled Cavity

The problem of deriving and solving equations for electro-

magnetic waves passing through a boundary is a difficult one, except

for simple cases, and, in general, only approximate solutions are

possible. An approach to the derivation of specific interest here is

by a method of virtual sources. For example, Huygen postulated

that a wave front could be visualized as a group of wavelets, i. e.,

virtual sources, which add together to produce a wave front. The

same principles can be applied here if the proper phases and

magnitudes are associated with each virtual source.

The specific problem formulated here is for active sources in a

dielectric which is bounded by a conducting surface on one side and

air on the other. The conducting surface will reflect all the incident

energy. At the dielectric-air boundary, the energy from an incident

wave is divided with part transmitted through the boundary and the

remainder reflected back into the dielectric.

It is obvious that there will be an infinite number of virtual sources, of various amplitudes and phases, induced on the boundary. For actual solution only a limited number of these sources, depending upon their respective amplitudes, are used. Figure 10 illustrates the number of 1st and 2nd order virtual sources set up at the boundary by the antenna's active region.

The notation convention selected for the derivation is as follows:

(1) The active region elements are noted as ℓ_1, ℓ_2, ℓ_3, and ℓ_4, with ℓ_2 as the resonant element,

(2) The virtual sources induced on the dielectric surface due to the active elements are noted as a_1, a_2, a_3, and a_4,

(3) The images of the active elements are noted as ℓ_1', ℓ_2', ℓ_3', and ℓ_4',

(4) The virtual sources induced on the dielectric surface due to the images of the active elements are noted as a_1', a_2', a_3', and a_4',

(5) The images of virtual sources a_1, a_2, a_3, and a_4 are noted as b_1', b_2', b_3', and b_4',

(6) The images of virtual sources a_1', a_2', a_3', and a_4' are noted as b_1', b_2', b_3', and b_4', etc.,

(7) The point on the surface directly above any element or image is noted as r_n where n = 1, 2, 3, or 4 for the respective element,
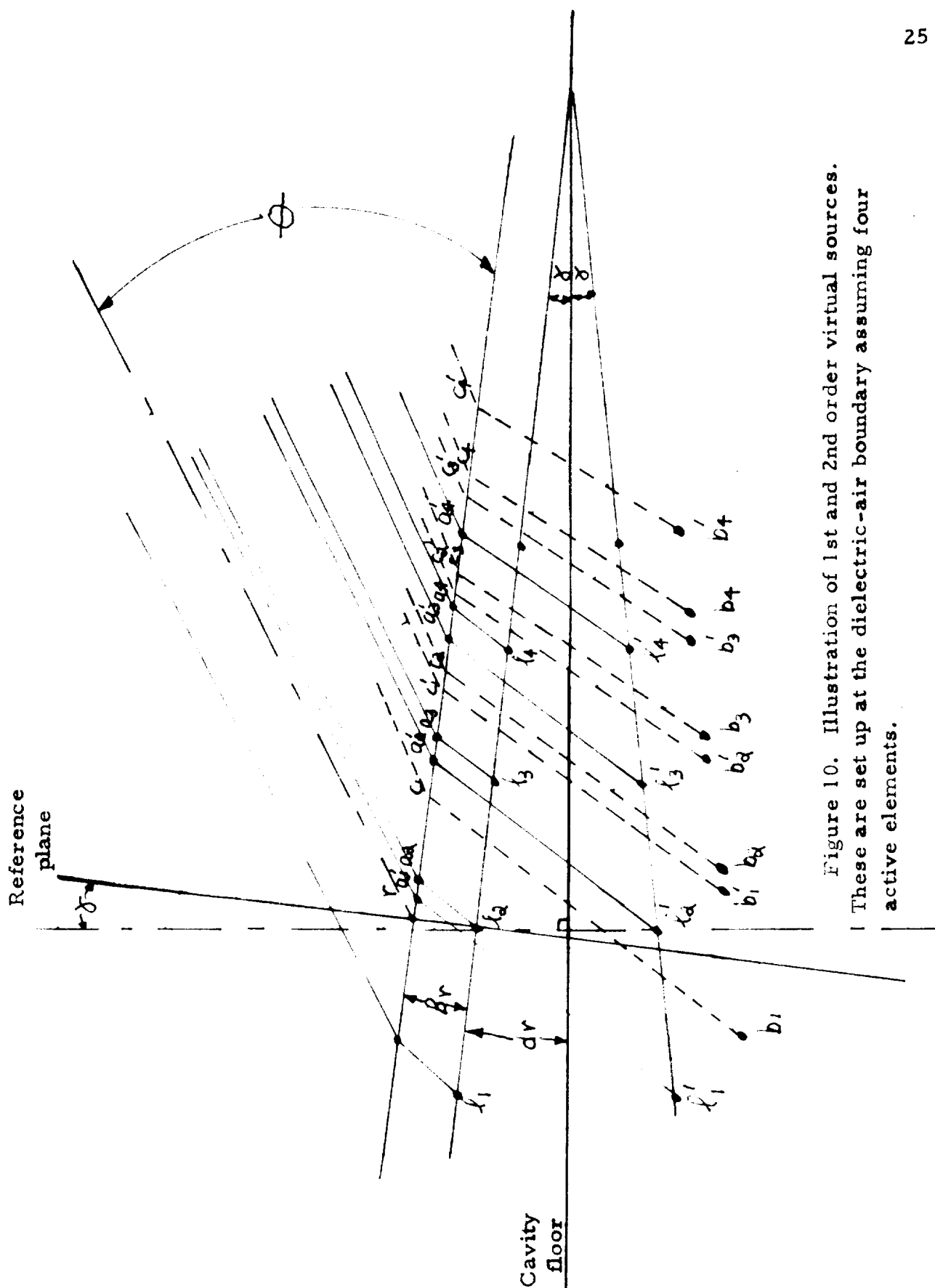
Figure 10.   Illustration of 1st and 2nd order virtual sources.
These are set up at the dielectric-air boundary assuming four
active elements.

(8) The radian phase distances between the line sources and the reference point r are noted as dn_1, dn_2, etc. This is the convention followed for the terms of the series of virtual sources. Point r is the point on the dielectric surface directly above the element λ_2, the resonant element.

Figure 11 shows the reference point r and the virtual sources on the boundary from the active elements, their images, and the images from this group (the original virtual sources).

The depth into the dielectric the antenna is submerged is B_r radians

$$\widehat{\lambda_1 r_1} = \frac{B_r}{\cos \phi} \tag{26}$$

where $\widehat{\lambda_1 r_1}$ = the radian distance between point $_1$ and point r_1.

By Snell's Law

$$\frac{\sin \phi}{\sin \phi'} = \frac{\sqrt{\mu_2 \epsilon_2}}{\sqrt{\mu_1 \epsilon_1}} = n$$

or $$\phi' = \sin^{-1} \left(\frac{1}{n} \sin \phi \right) \tag{27}$$

$$\widehat{\lambda_1 a_1} = \frac{B_r}{\cos \phi'} = \frac{B_r}{\cos \left[\sin^{-1} \left(\frac{1}{n} \sin \phi \right) \right]}$$

$$a_{11} \equiv \widehat{a_1 r} = \widehat{r_1 r} - \widehat{r_1 a} = 2\pi \left(\frac{1}{\tau} - 1 \right) - \widehat{l_1 a_1} \sin \phi'$$

$$= 2\pi \left(\frac{1}{\tau} - 1 \right) - B_r \tan \left[\sin^{-1} \left(\frac{1}{n} \sin \phi \right) \right] \tag{28}$$
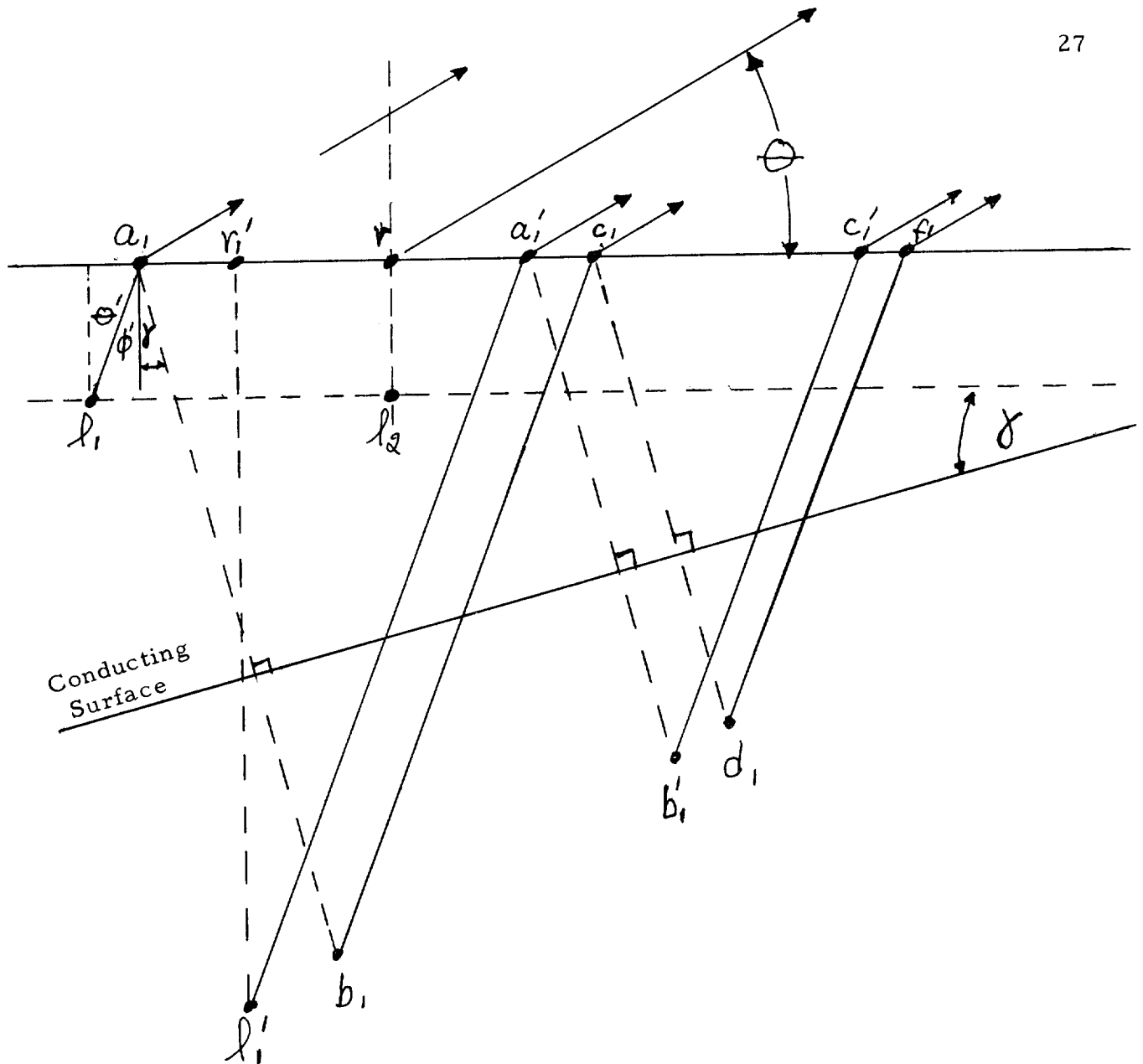
Figure 11. A single source and its induced virtual sources. This is an illustration of how an active element, ℓ_1, induces an infinite number of virtual sources on the boundary via complete reflection of the wave at the conducting surface and partial reflection of the wave at the dielectric-air boundary.

The field produced by element ℓ_1 is split as it passes the boundary and only a portion of it continues into the next medium (air). The field contributed at point p (the observation point) from virtual source a_1 is $E_{a_1} = A E_o e^{-j\psi_{a_1}}$ where A is the transmitted fraction of the energy and $\psi_{a_1} = a_{11} \cos\theta + b_{a_1}$ and b_{a_1} is the phase lag of a_1 with respect to point r.

The reflected portion of the wave from virtual source a_1 will induce the image b_1. The image b_1 will be the source of virtual source c_1 on the dielectric surface. Referring to Figure 11, it is obvious that the position of source b_1 is a function of θ since the position of a_1 is a function of θ. By use of geometrical relations the phase distance of c_1 with respect to point r, can be expressed as

$$c_{11} = \frac{\sin(\gamma + \phi')}{\cos\phi'}\left\{\frac{2 B_r}{\cos\phi'} \cos(\phi' + \gamma) + 2dr + 4\pi\left(\frac{1}{\tau} - 1\right)\sin\gamma\right\}$$
$$-2\pi\left(\frac{1}{\tau} - 1\right) + B_r \tan\phi' \qquad (30)$$

Where ϕ' may be expressed in terms of ϕ or θ as previously noted. The field contribution by this virtual image is

$$\bar{E}_{c_1} = A B E_o e^{j\psi_{c_1}} \qquad (31)$$

where A is the transmitted fraction of the wave incident at point c_1 and B is the relative magnitude of the source b_1 to ℓ_1.

$$\psi_{c_1} = c_{11} \cos \theta + b c_1$$

where b_{c_1} is the phase lag of c_1 with respect to r.

The reflected portion of the wave from the point c_1 will induce image d_1. This in turn sets up the virtual source f_1 (see Figure 11). This process continues indefinitely, with each successive source being only a fraction of the amplitude of the previous source. Expressions similar to equation (31) may be set up for these successive virtual sources.

The energy wave directed from ℓ_1 perpendicular to the cavity floor may be analyzed as an "image" source ℓ'_1 (see Figure 11). The position of l'_1, unlike all the other images induced by the virtual sources on the boundary, does not change with θ but only with the cavity floor angle γ.

Source l'_1 induces virtual source a'_1 at the boundary which has a position which is a function of θ. From the geometry of Figure 11, the phase distance of a'_1 with respect to r can be expressed as

$$a'_{11} = \frac{\sin(\phi' + \gamma)}{\cos \phi'} \left[2dr + 4\pi \left(\frac{1}{\tau} - 1\right) \sin \gamma + \frac{B_r}{\cos \gamma} \right] - 2\pi \left(\frac{1}{\tau} - 1\right) - B_r \tan \gamma \qquad (32)$$

The contribution to the field at point p (the observation point) from virtual source a'_1 is

$$E_{a_1} = A E_o e^{j \psi_{a_1}} \tag{33}$$

where $\qquad \psi_{a_1} = a_{11} \cos \theta + \delta_{a'_1}$

$A =$ the fraction of energy transmitted at the boundary

$E_o =$ the magnitude of the field from source ℓ_1 which

would necessarily be there if no boundary existed.

Since a fraction of the energy is reflected and induces a second

image, there will be an infinite series of virtual sources set up by

the "prime" image source ℓ_1, that is, similar to the series created

by direct ray from ℓ_1.

The total contribution of ℓ_1 to the far field is the summation of

all the individual virtual sources on the boundary which are induced

by ℓ_1 and its image ℓ'_1. Mathematically

$$\overline{E}_{1_1} = \overline{E}_{a_1} + \overline{E}_{c_1} + \overline{E}_{F_1} + \ldots + \overline{E}_{a'_1} + \overline{E}_{c'_1} + \overline{E}_{F'_1} + \ldots$$

or $\quad E_{1_1} = A E_o (e^{j \psi_{a_1}} + B e^{j \psi_{c_1}} + Bc\, e^{j \psi_{F_1}} + \ldots + e^{j \psi_{a'_1}}$

$$+ B e^{j \psi_{c'_1}} + Bc\, e^{j \psi_{F'_1}} + \ldots) \tag{34}$$

The series described here must converge for physical reasons

since some energy must be transmitted at each virtual source on the

air-dielectric boundary. The rapidity with which the series converges

is dependent upon the angle θ and the ϵ_r of the dielectric material;

i.e., the higher dielectric constant material reflects more energy

than the lower dielectric constant material. The greater ϕ is, the

more the reflected energy.

Further evaluation of this equation will await programming

for the Utah State University IBM 1620 computer. Such a program

is planned and is essential if the very large number of calculations

are to be performed in a reasonable time.

EXPERIMENTATION

Procedure

The log-periodic monopole antennas used in the experimental

portion of this study are shown in Figures (12a), (12b), and (12c).

Each antenna was designed for upper and lower cutoff frequencies

of 4.0 Gc and 2.0 Gc respectively. They were assumed to be sub-

merged in dielectric. The design was accomplished by setting the

length of the longest and shortest elements at 0.25λ where λ is the

wave length of the lowest or highest frequency of the desired range,

(2.0 to 4.0 Gc). The distance from the apex to the resonant element

was chosen to be λ_n, the wave length of the excitation frequency.

This determined the antenna's taper angle since

$$\alpha = \tan^{-1} \frac{l_n}{S_n} = \tan^{-1} \frac{0.25\,\lambda_n}{\lambda_n} = 14^{\circ}$$

The logarithmic ratio τ was chosen to be 0.85 which determined the

spacing between the elements.

The antennas were constructed of 1/16 inch diameter copper

rods with elements soldered onto a center rod.

The cavity dimensions were as shown in Figures (13a), (13b), and

(13c). For each cavity the perpendicular distant from the cavity floor

Figure 12a. Dimensions of log-periodic monopole antenna, ϵ = 1.0. Antenna designed with α = 14°, τ = 0.85, and frequency range 2.8 Gc to 4.0 Gc. Dimensions shown in cm.
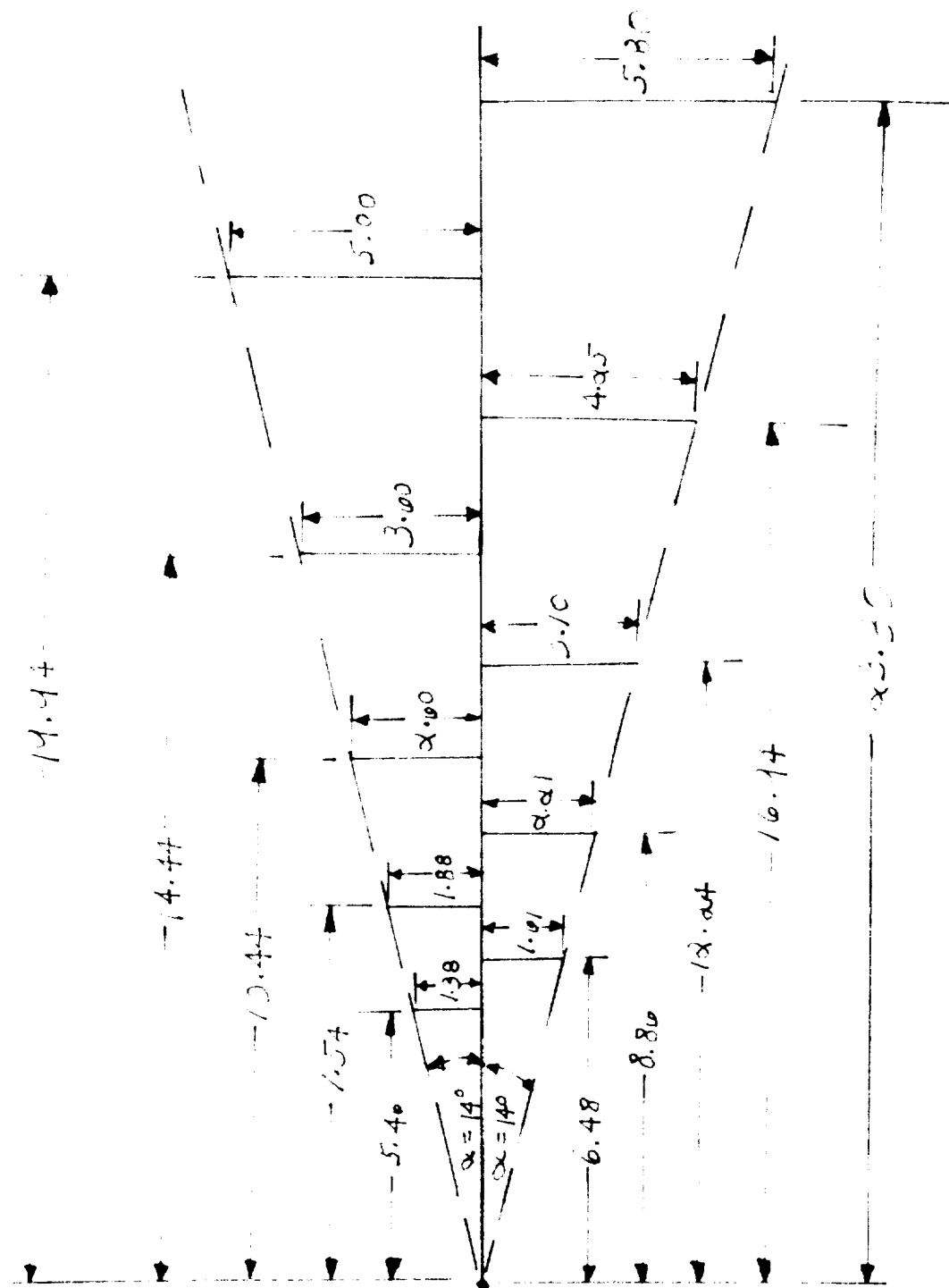
Figure 12b. Dimensions of log-periodic monopole antenna, ϵ_r = 2.25. Antenna designed with α = 14°, τ = 0.85, and frequency range 2.0 Gc to 4.0 Gc. Dimensions shown in cm.

Figure 12c. Dimensions of log-periodic monopole antenna, α = 4.0.
Antenna designed with α = 14°, τ = 0.85, and frequency range 2.0 c to 4.0 c.
Dimensions shown in cm.

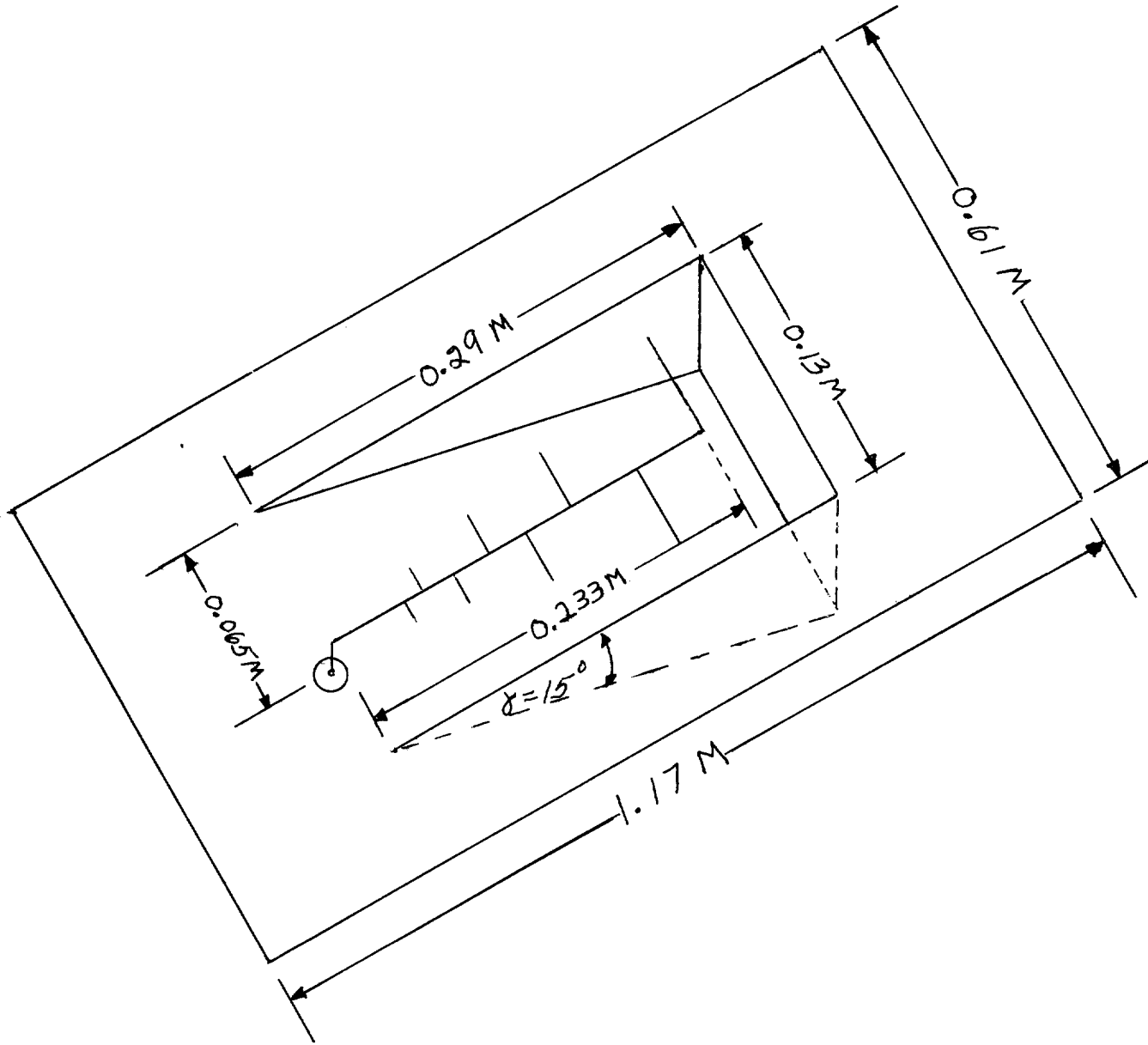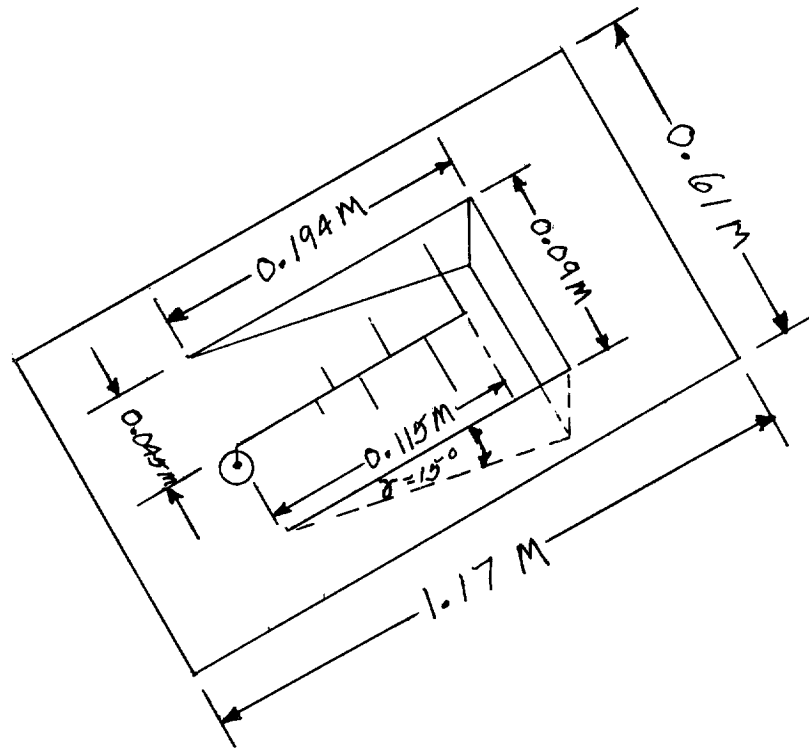Figure 13a. Perspective view of cavity, $\epsilon_r = 1.0$. Antenna is shown in mounted position.

Figure 13b. Perspective view of cavity, ϵ_r = 2.25. Cavity is shown without dielectric cover. Cavity dimensions are noted.
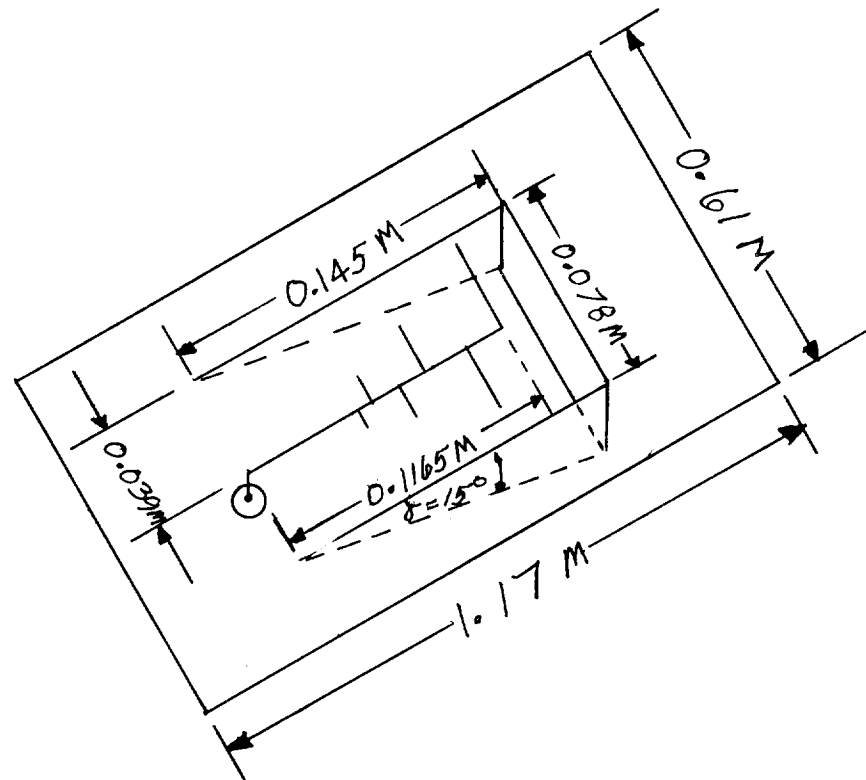

Figure 13c. Perspective view of cavity, ϵ_r = 4.00. Cavity is shown without dielectric cover. Cavity dimensions are noted.

to the active antenna element was designed to be $0.25 \lambda_n$. The distance

from the longest element to the back wall of the cavity was chosen to be

$0.25 \lambda_L$. Previous investigation by Clark, Jones, and Leigh, (1962)

indicated that the spacing of the antenna relative to the back and side

walls of the cavity, if not too small, have negligible effects upon the

characteristics of the radiating structure.

The cavities were constructed of brass sheets. The sheet size was

sufficient to allow the sheet to extend in all directions at least 1 wave

length at the lowest frequency.

From the three basic cavities, radiation field patterns of the E-

and H-planes and driving point impedances were measured.

These radiation field patterns were measured on a standard

antenna pattern range. The superheterodyne detection system shown

in Figure 14 was used. The resulting patterns are relative field inten-

sity (linear voltage) plots. The coordinate system of Figure 16 was used.

The driving point impedances were measured for the structures by the

slotted line methods described by Smith (1944). The impedance test

setup is shown in Figure 15.

Results

The experimental results presented here were obtained from models

described in Figures (13a), (13b), and (13c).

Normalized plots of impedance vs. frequency for $\epsilon_r = 1.00, 2.25,$

and 4.00 are presented in Figures 17 through 19.

Figure 14. Pattern measurement arrangement.
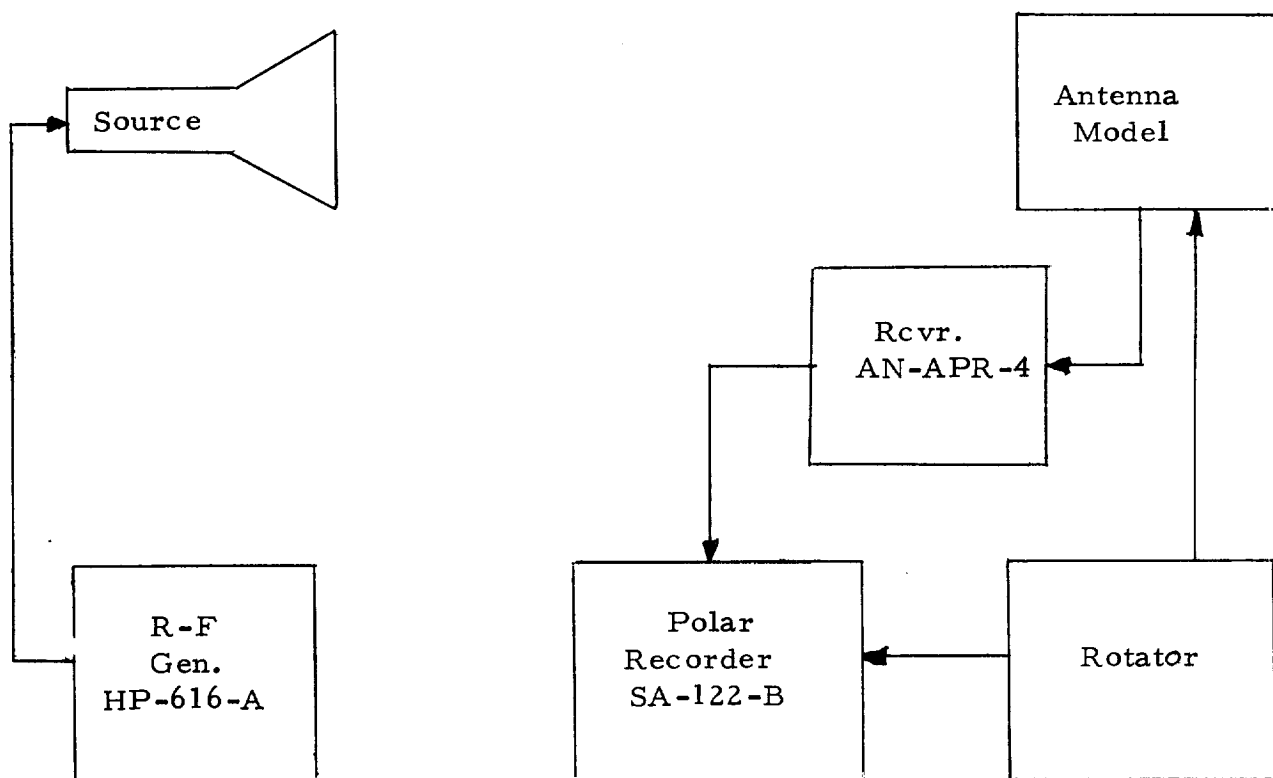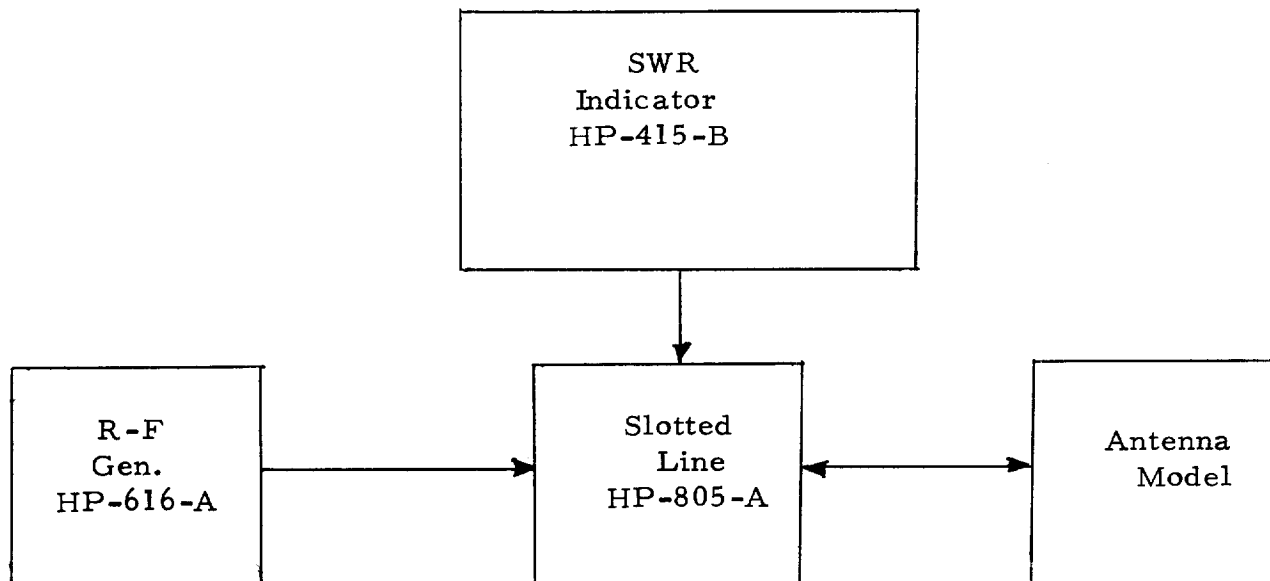

Figure 15. Impedance measurement arrangement.
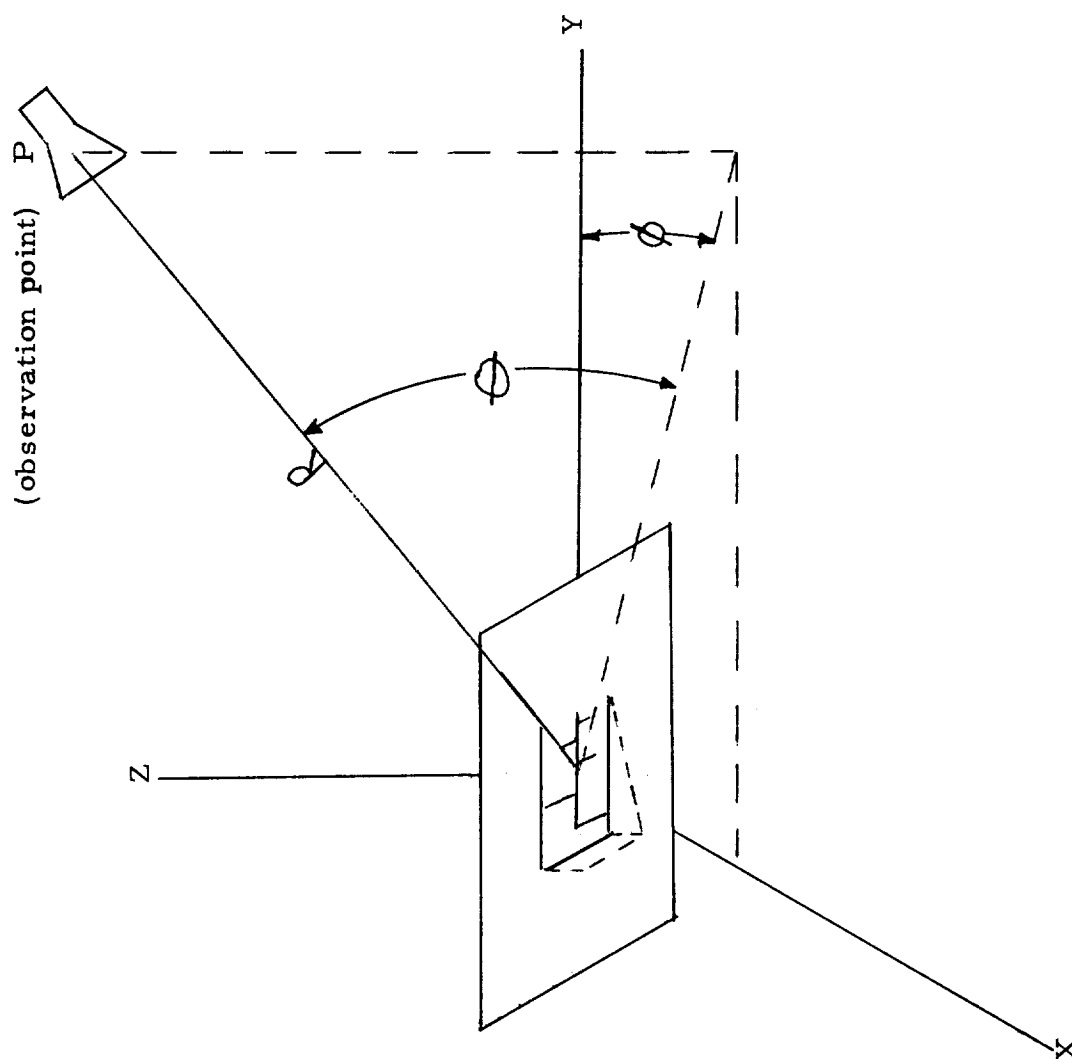
Figure 16. Coordinate system for radiation field measurements.
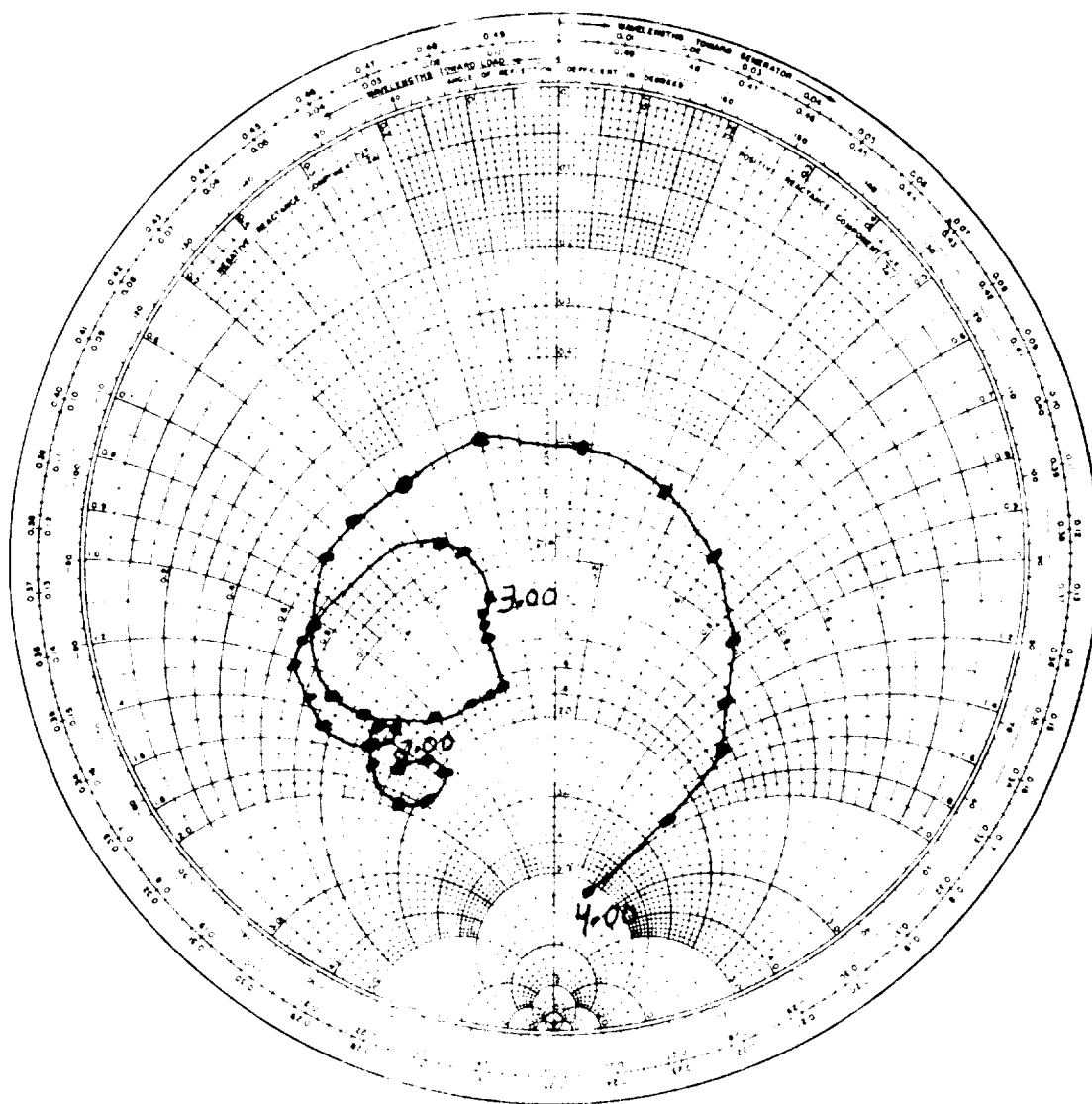
Figure 17. Antenna impedance, $\epsilon_r = 1.0$. The impedance is normalized to 50 ohms. Frequencies are shown in Gc.
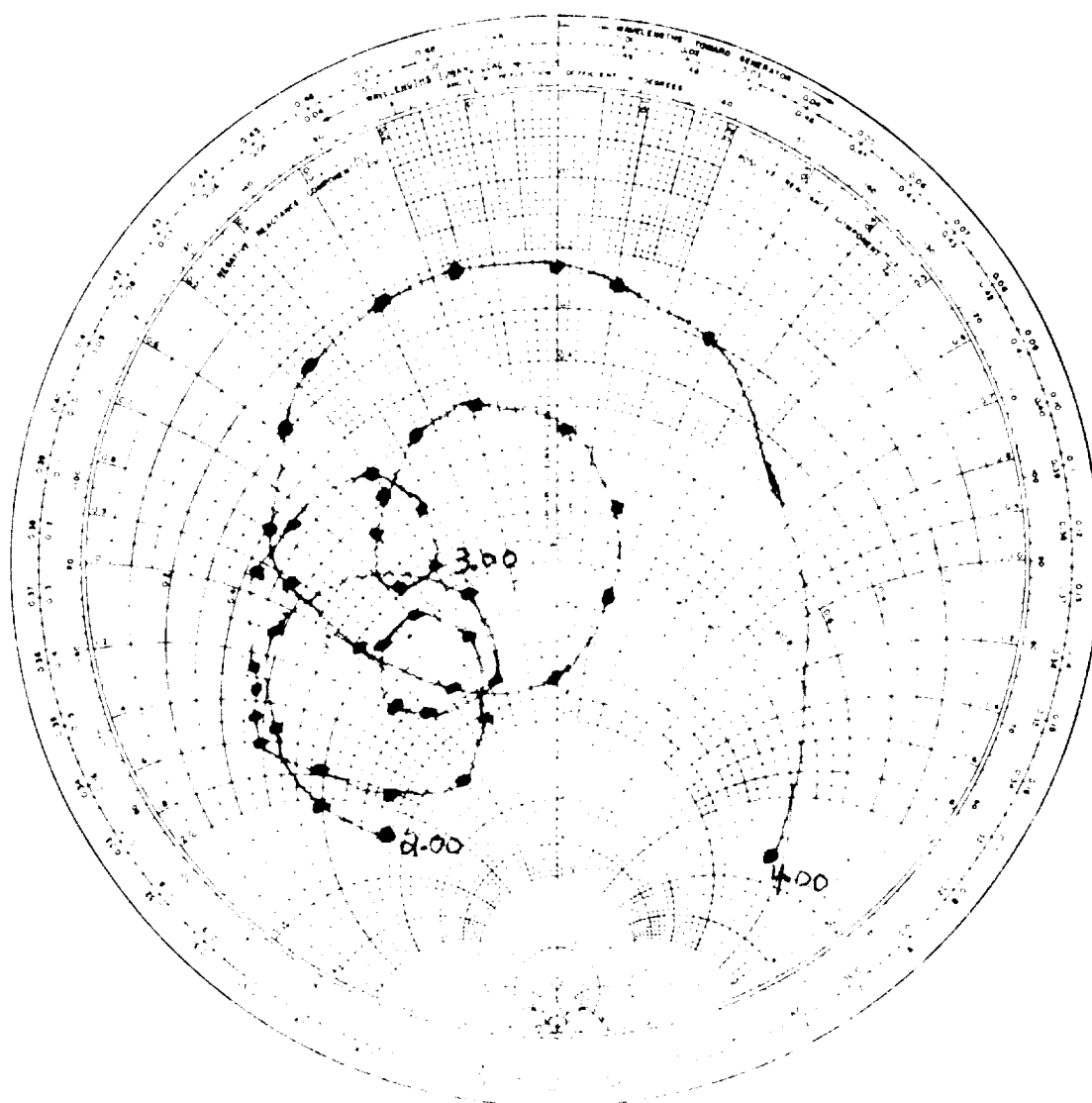
Figure 18a. Antenna impedance, ϵ_r = 2.25. Dielectric cover thickness = 3/16 inch. The impedance is normalized to 50 ohms. Frequencies shown in Gc.
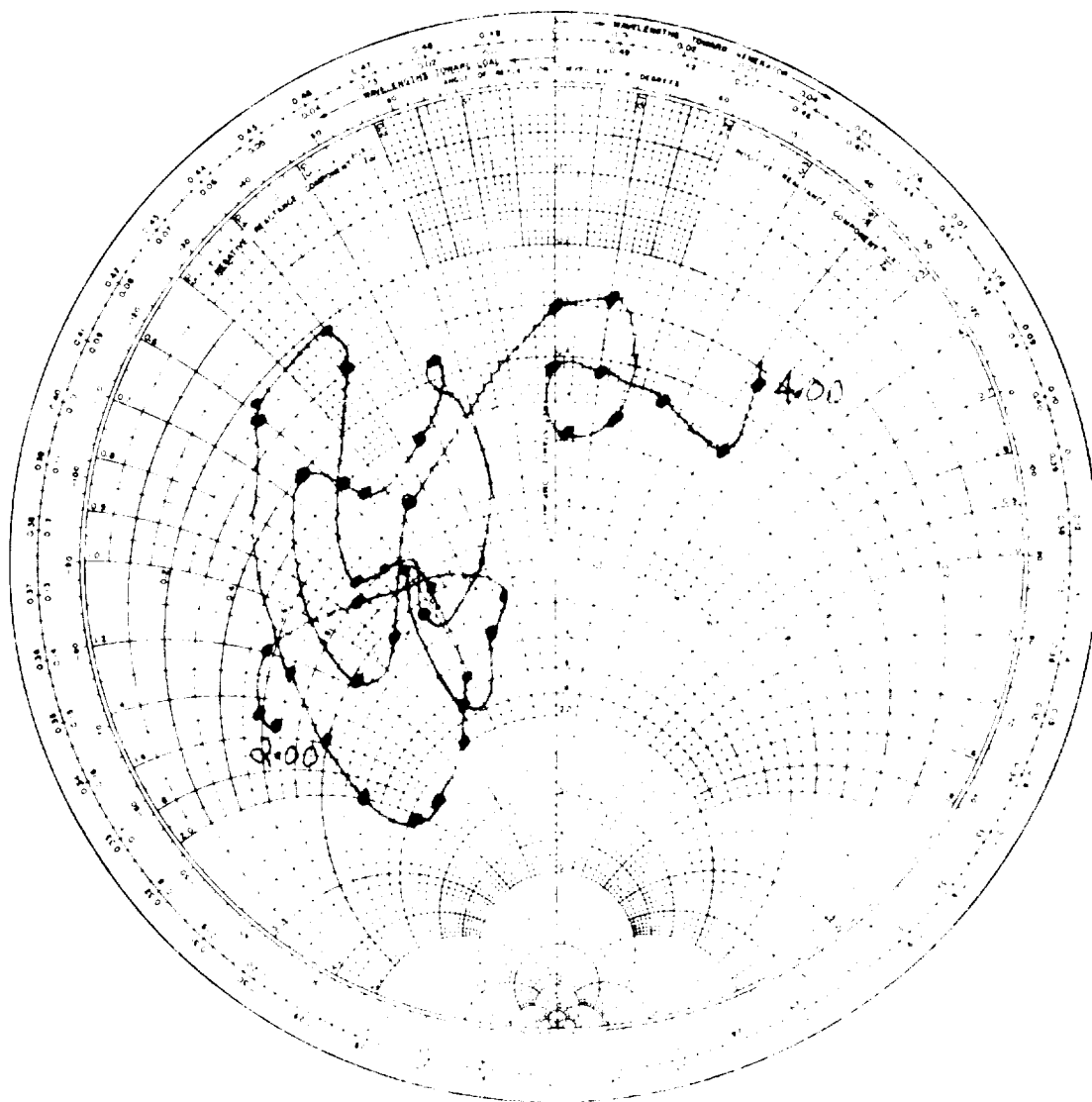
Figure 18b. Antenna impedance, ϵ_r = 2.25. Dielectric cover thickness = 5/16 inch. The impedance is normalized to 50 ohms. Frequencies shown in Gc.
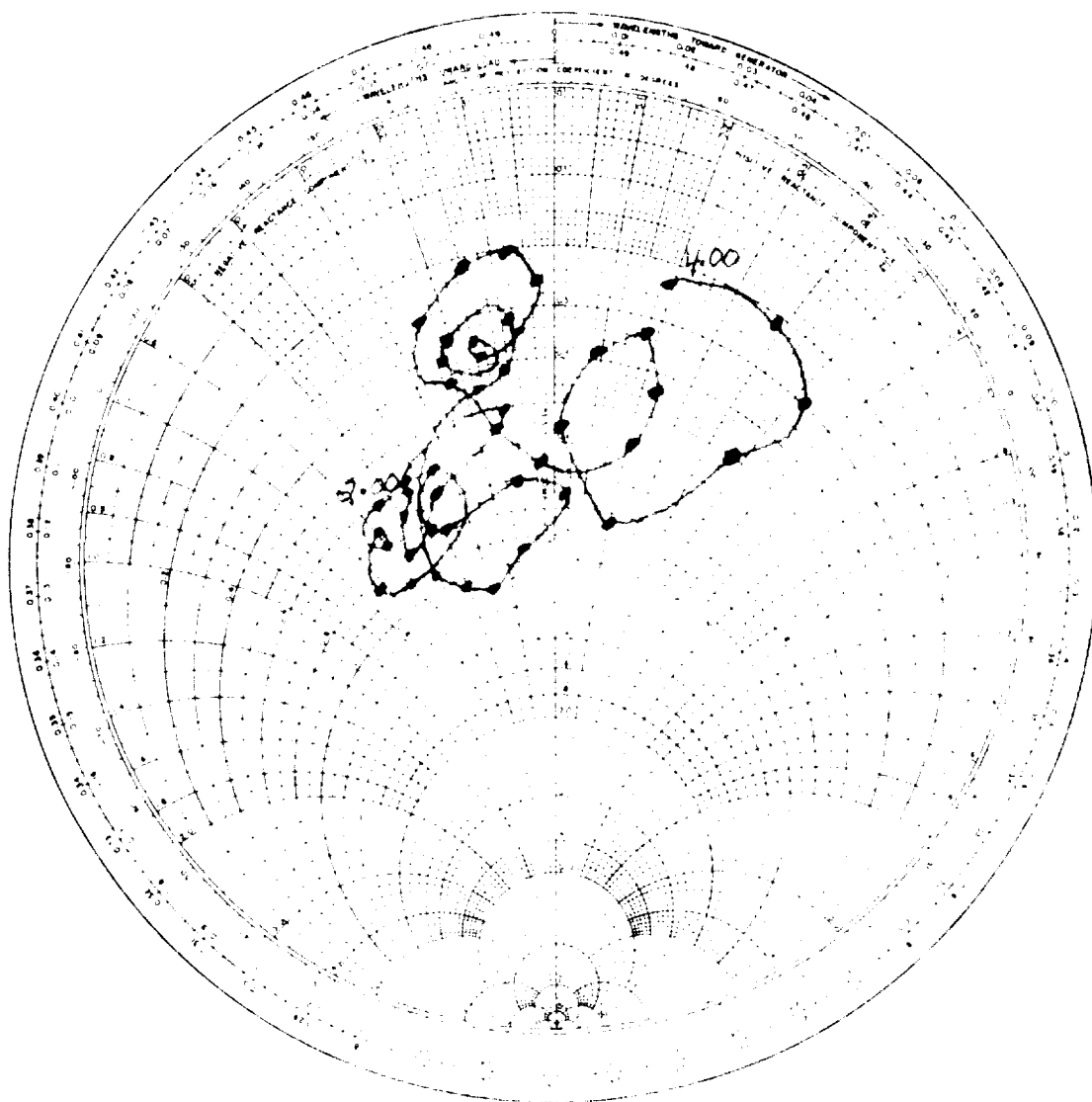
Figure 19. Antenna impedance, ϵ_r = 4.0. Dielectric cover thickness = 9/32 inch. The impedance is normalized to 50 ohms. Freq. is shown in Gc.

Typical experimental radiation patterns are presented in Figures 20 through 23. Tables 1 through 3 present specific information on all measured radiation patterns of the three model variations at various frequencies.
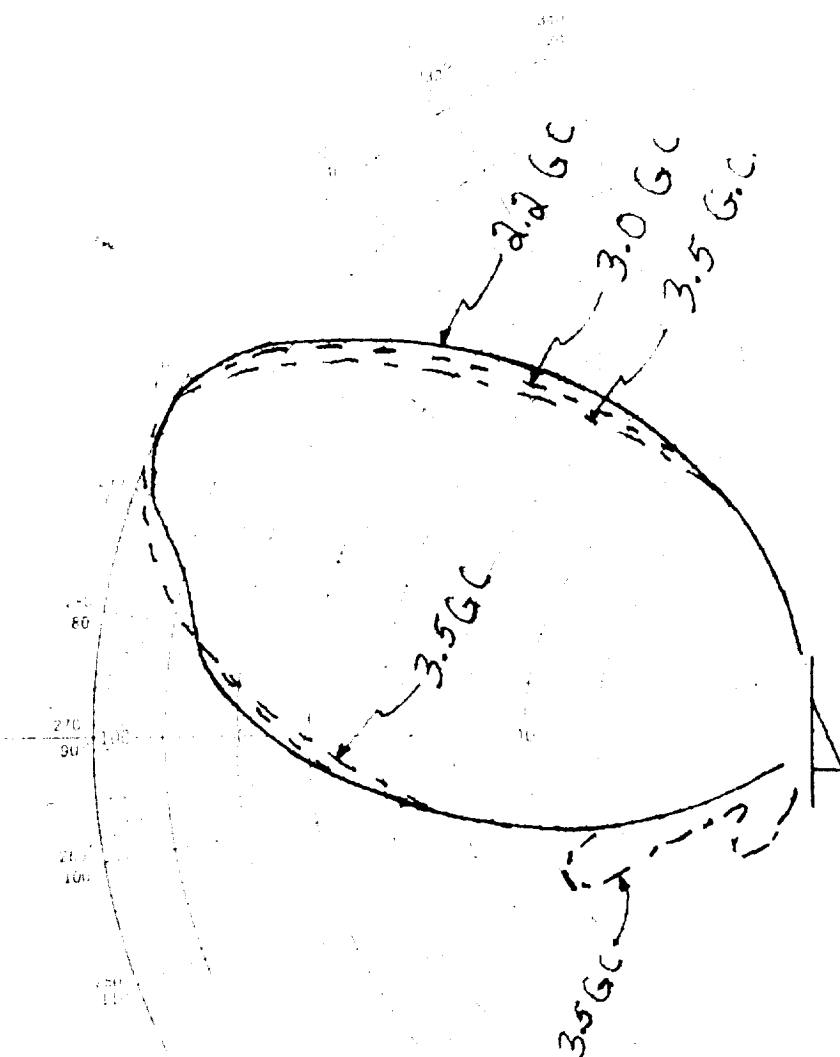
Figure 20a. H-plane pattern Vs. frequency, ϵ_r = 1.0. Linear voltage plot of an antenna-cavity assembly with ϕ = 0°, θ = variable.
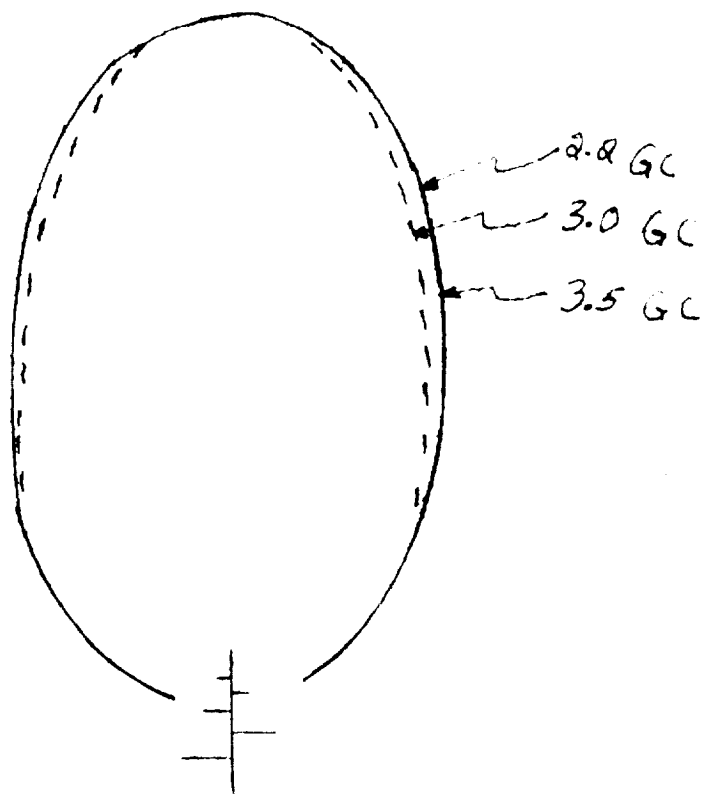
Figure 20b. E-plane pattern Vs. frequency, $\epsilon_r = 1.0$. A linear voltage plot of an antenna-cavity assembly with $\phi = 0°$, θ = variable.
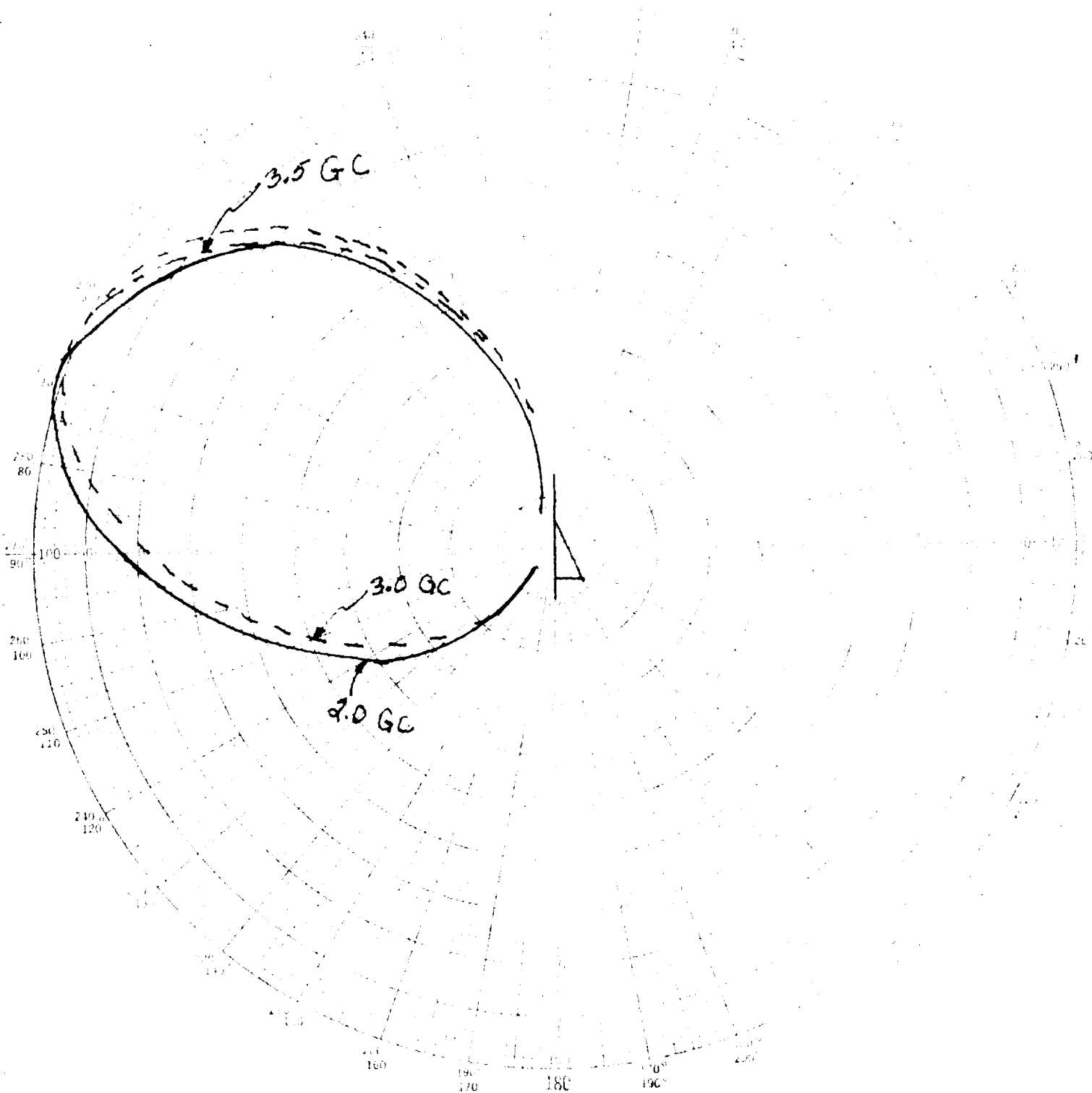
Figure 21a. H-plane pattern Vs. frequency, $\epsilon_r = 2.25$.
Linear voltage plot.
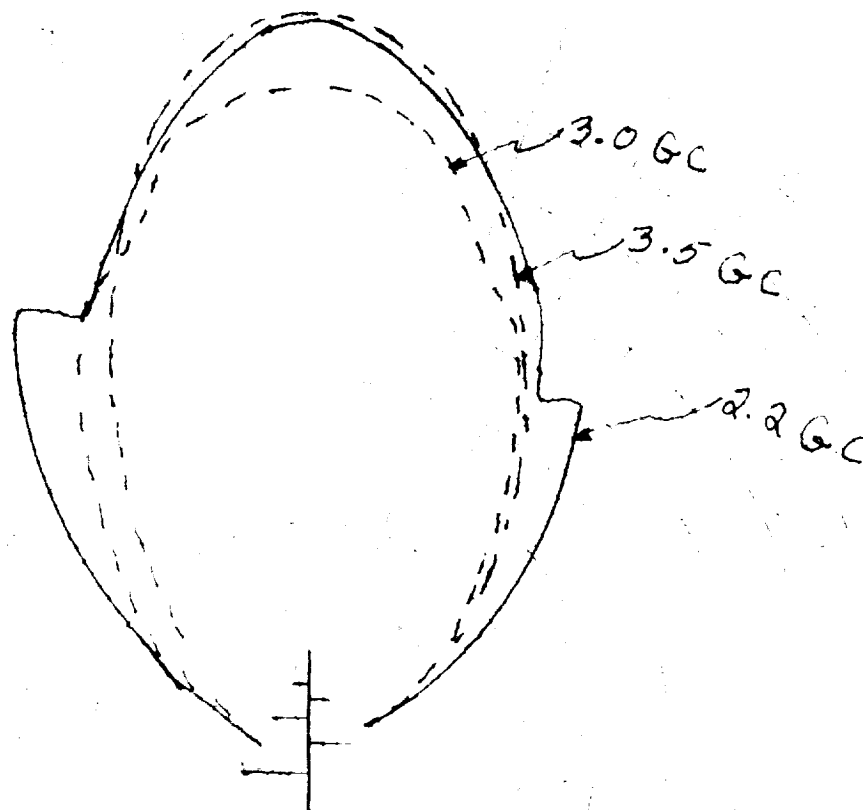
Figure 21b.   E-plane pattern Vs. frequency, ϵ_r = 2.25.
A linear voltage plot.
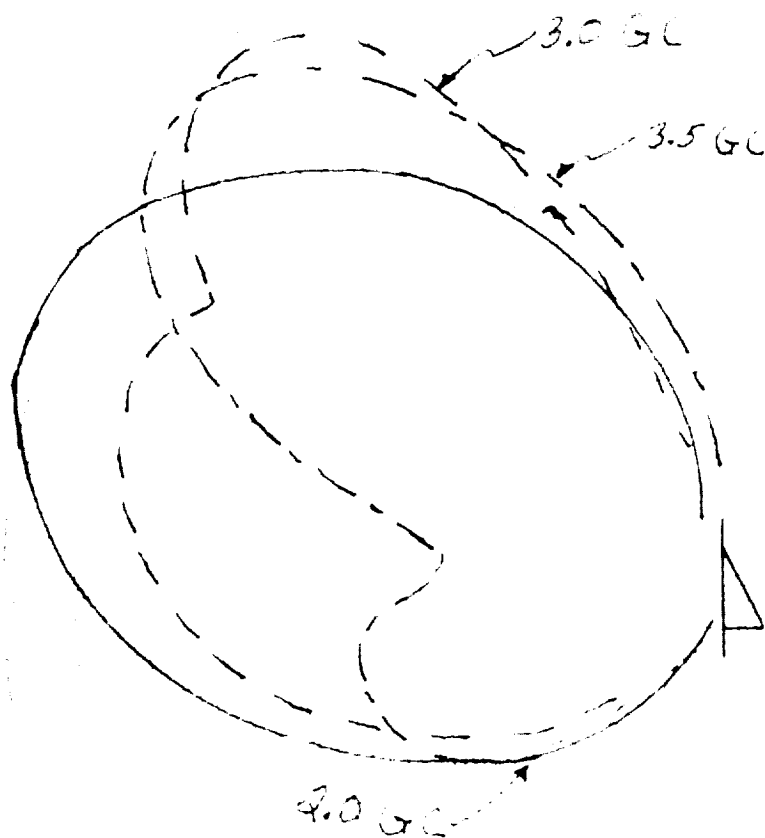
Figure 22a. H-plane pattern Vs. frequency, $\epsilon_r = 4.0$.
A linear voltage plot.
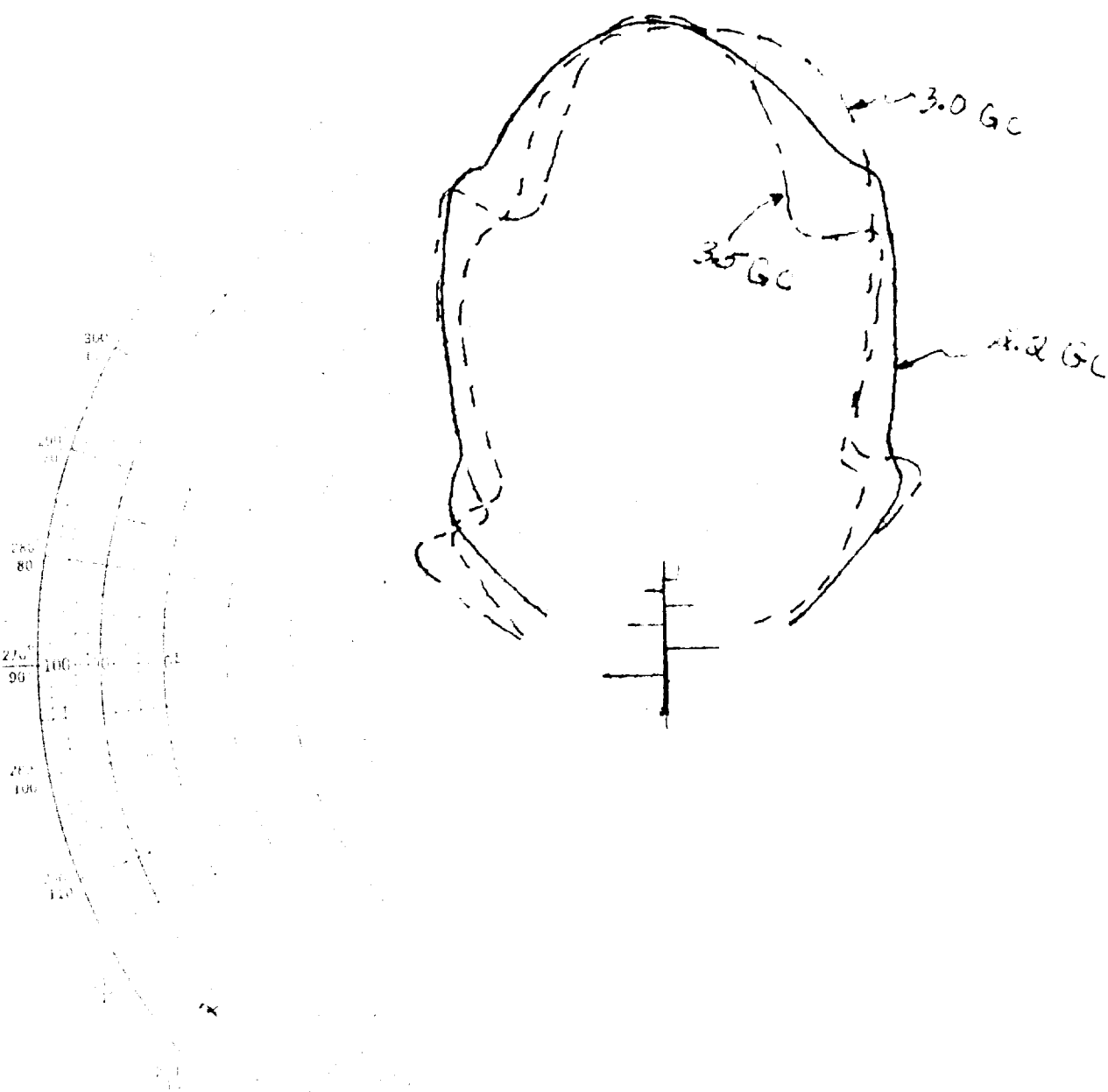
Figure 22b. E-plane pattern Vs. Frequency, $\epsilon_r = 4.0$.
A linear voltage plot.
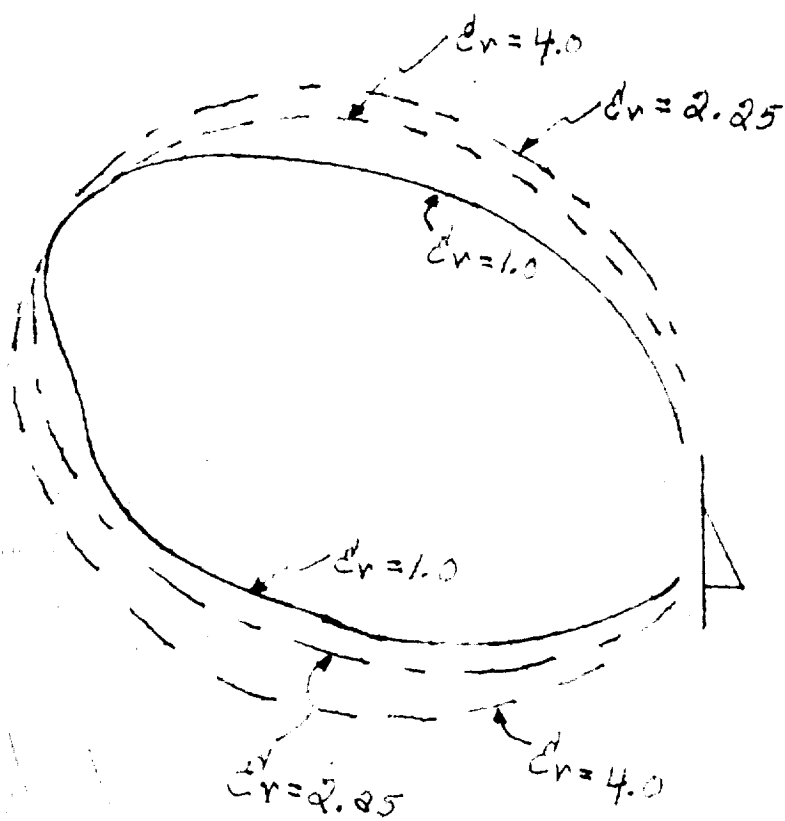
Figure 23a. H-plane patterns Vs. ϵ_r. A linear voltage plot with frequency = 2.2 Gc.
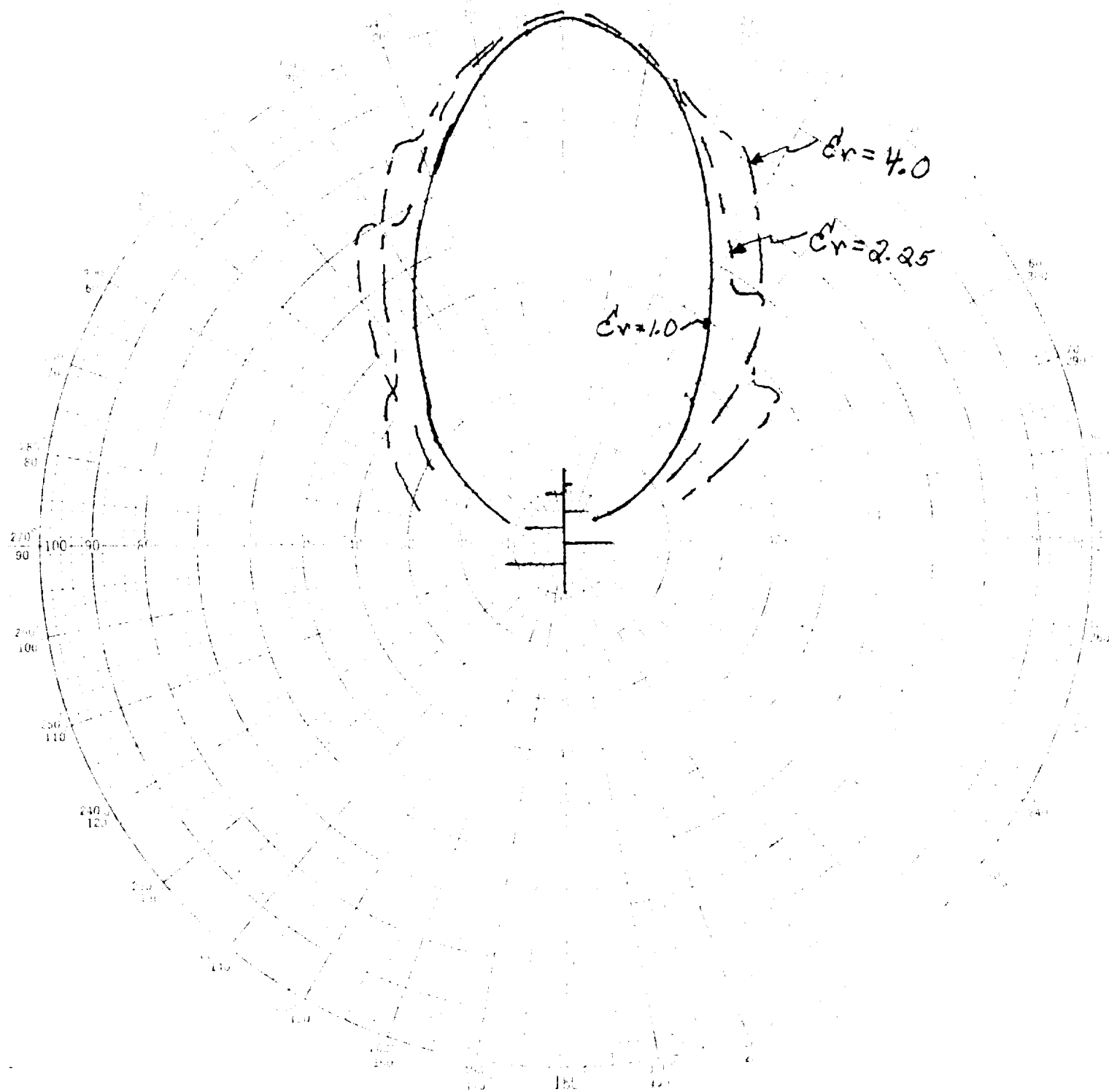
Figure 23b.   E-plane patterns Vs. ϵ_r.   A linear voltage
plot with frequency = 2.2 Gc.

Table 1a. H-plane radiation data, $\epsilon_r = 1.0$.

Frequency	Observation of Radiation Lobes	Comments
2.2 Gc	Main lobe 65° 1/2 power points 90° and 45°	No side lobes
2.5 Gc	Main lobe $65^{\circ} - 70^{\circ}$ 1/2 power points 92° and 47°	No side lobes
3.0 Gc	Main lobe $65^{\circ} - 65^{\circ}$ 1/2 power points 90° and 45°	No side lobes
3.5 Gc	Main lobe $60^{\circ} - 65^{\circ}$ 1/2 power points 90° and 45°	Side lobes forming at 120° and 155°
4.0 Gc	Main lobe 60° 1/2 power point 100° and 35°	Large side lobes at 120° and 150° (Considerable noise on pattern)

Table 1b. E-plane radiation data, $\epsilon_r = 1.0$.

Frequency	Observation of Radiation Lobes	Comments
2.2 Gc	Main lobe 0° 1/2 power points $\pm 22^{\circ}$	
2.5 Gc	Main lobe 0° 1/2 power points $\pm 23^{\circ}$	
3.0 Gc	Main lobe 0° 1/2 power points $\pm 20^{\circ}$	
3.5 Gc	Main lobe -5° 1/2 power points $\pm 22^{\circ}$	
4.0 Gc	Main lobe 0° 1/2 power points $\pm 22^{\circ}$	

Table 2a. H-plane radiation data, $\epsilon_r = 2.25$.

Frequency	Observation of Radiation Lobes	Comments
2.2 Gc	Main lobe $65^{\circ} - 70^{\circ}$ 1/2 power points 95° and 30°	No side lobes
2.5 Gc	Main lobe $65^{\circ} - 70^{\circ}$ 1/2 power points 95° and 30°	
3.0 Gc	Main lobe $65^{\circ} - 70^{\circ}$ 1/2 power points 95° and 30°	
3.5 Gc	Main lobe $60^{\circ} - 65^{\circ}$ 1/2 power points 95° and 35°	
4.0 Gc	Main lobe $65^{\circ} - 70^{\circ}$ 1/2 power points 90° and 45°	Main lobe has sharpened up considerably but no side lobes

Table 2b. E-plane radiation data, $\epsilon_r = 2.25$.

Frequency	Observation of Radiation Lobes	Comments
2.2 Gc	Main lobe 0° 1/2 power points $\pm 28^{\circ}$	
2.5 Gc	Main lobe 0° 1/2 power points $\pm 28^{\circ}$	
3.0 Gc	Main lobe 0° 1/2 power points $\pm 30^{\circ}$	
3.5 Gc	Main lobe 0° 1/2 power points $\pm 25^{\circ}$	
4.0 Gc	Main lobe 0° 1/2 power points $+20^{\circ}$ and -30°	Side lobes formed Not symmetrical about 0°

Table 3a. H-plane radiation data, $\epsilon_r = 4.0$.

Frequency	Observation of Radiation Lobes	Comments
2.2 Gc	Main lobe 70° 1/2 power points 105° and 35°	
2.5 Gc	Main lobe 70° 1/2 power points 105° and 38°	
3.0 Gc	Main lobe 40° 1/2 power points 105° and 25°	Lobe at 40° was about 2db larger than the lobe at 75°
3.5 Gc	Main lobe 50° 1/2 power points 68° and 28°	Side lobes at 105° with its 1/2 power points at 130° and 75°. Peak is about 7db below main lobe.
4.0 Gc	Main lobe 30° 1/2 power points 40° and 13°	Side lobes at 95° and 128°. 1/2 power points: 80° and 105°; 120° and 130°. About 2db and 7db below main lobe.

Table 3b. E-plane radiation data, ϵ_r = 4.0.

Frequency	Observation of Radiation Lobes	Comments
2.2 Gc	Main lobe 0° 1/2 power points $\pm$ 50°	Small side lobes at $+25^{\circ}$, $+55^{\circ}$, -25°, -55°
2.5 Gc	Main lobe 0° 1/2 power points $\pm$ 35°	Slight side lobes
3.0 Gc	Main lobe 0° 1/2 power points $\pm$ 30°	Slight side lobes
3.5 Gc	Main lobe 0° 1/2 power points $\pm$ 15°	Side lobes at $+25^{\circ}$, $+55^{\circ}$, -25°, and -65°. These are about 1.5 db below main lobe.
4.0 Gc	Main lobe $+20^{\circ}$ 1/2 power points $+35^{\circ}$ and -5°	Negligible side lobes

DISCUSSION AND CONCLUSIONS

In this part of the report, the experimental results are summarized and discussed.

In a previous section, the H-plane radiation equation, equation (21), was derived for an air dielectric cavity and evaluated for different values of the elevation angle θ. The close agreement of the calculated pattern with the measured radiation pattern (see Figure 9) illustrates that the approximations made for the analysis were nearly correct. Similar approximations may hold true when the antenna is submerged in a dielectric medium.

Three important assumptions about the antenna are verified by the agreement of the calculations with the measured pattern. These are:

(1) The active region of the antenna can be determined by estimating the base impedance of each element, at the operating frequency, and thus determine the contributions of each element to the radiation pattern,

(2) The center bar of the antenna acts as a transmission line,

(3) The velocity of the voltage wave on the center bar is approximately uniform over the active region.

Figures 21 and 22 show that, for the models in which $\epsilon_r = 1.0$ and $\epsilon_r = 2.25$, the directions and shapes of the antenna's radiation

lobes vary slightly with a change of frequency but they are essentially
independent of frequency.

The radiation patterns for the model in which ϵ_r = 4.0 (Figure 22a),
while still a broadband antenna, did not show frequency independent
radiation characteristics as effectively as the other models. A
possible reason for this may be in the precision of construction of the
antenna. For this dielectric constant, the physical size of the antenna
is much smaller than the previous two models, as shown in Figures 13
and 14. Precision of construction is important to insure proper phase
relations between the elements. Further investigation is needed to
determine the design criterion necessary to permit full "frequency
independent" performance from log periodic antennas immersed in
high permittivity dielectrics.

The side lobes for the E-plane patterns shown in Figure 22b are
also noted to occur in the patterns for the antenna model in which
ϵ_r = 2.25 (Figure 21b). The cause of this is perhaps related to the
dielectric cover. Inspection of Figure 3a shows that the dielectric cover
used over the antenna after the antenna was fitted in the cavity protrudes
slightly above the surface of the brass sheet. It is possible that energy,
reflected around in the dielectric, could emerge in small amounts through
the side of the dielectric which is not within the cavity.

In Figures 20 through 22, 3.5 Gc is shown as the highest frequency
used for the radiation patterns. Observation of the Tables will indicate
that at 4 Gc the patterns of each model are not similar to the previous

patterns. The number of elements composing the active region is not the same at 4.0 Gc as at lower frequency. As noted in the theory, the highest frequency of operation is determined by the length of the shortest element. The shortest element is resonant at 4.0 Gc and shorter elements are not practical in this design. Since the active region, for the τ and α selected for this investigation, consisted of four elements, operation at 4.0 Gc changes the active region from four elements to two elements. With this change in the active region, the radiation patterns and driving point impedances are expected to deviate from the measurements made at lower frequencies.

A fourth item of importance is illustrated in Figure 22a and 22b. Comparison of the radiation patterns (both E- and H-planes), for a constant frequency but different dielectric materials, shows that the beam width increases with an increase in the relative dielectric constant, ϵ_r. The exact analytic explanation for this beam broadening effect is not presently possible, but certain general points, which determine the pattern, should be discussed.

The general radiation pattern is determined by the amplitudes and relative phases of all virtual sources along the dielectric-air boundary. There is an infinite number of these virtual sources on the boundary and only those of significant amplitude have any important effect upon the radiation pattern. With an increase in the dielectric constant of the medium, the number of significant virtual sources increases. This is because the reflected energy at the boundary is larger with higher

dielectric constant. Associated with the virtual source amplitudes are the various phases. These phases are determined by the propagation path lengths to each of the virtual sources from the active antenna element which caused it.

The beam width of the antenna can be changed (narrowed or widened) by controlling the phase of each virtual source. The number of virtual sources and the amplitude of each is determined by the dielectric constant of the material filling the cavity. It appears that in the examples of this study the phases of the various virtual sources are not in the optimum phases for maximum beam sharpness. The phase relations between these virtual sources can be changed by changing the cavity floor angle γ. An investigation into control of the beam width by this method is suggested and could yield an improved cavity design for minimum beam width.

The plots of the driving point impedances for the various antenna-cavity models (Figures 17 through 19) show that the impedance characteristics essentially repeat periodically when submerged in a dielectric. The general impedance spirals shown are in the general area of low VSWR; thus it can be expected to operate effectively on a system which has a 50 ohm feed line.

To investigate experimentally the effects of the dielectric cover thickness, one antenna model was constructed with two different covers. The radiation patterns taken with these two covers were nearly identical. Therefore, they were not recorded in this report. The driving point

impedances measured with the two different covers differed slightly

in the spiral characteristics (Figures 18a and 18b), but they still

presented essentially the same impedance variation.

The advantages inherent in an increased dielectric constant material

is the reduced physical size of the antenna and cavity. The floor angle

of the cavity, δ, remains constant for any ϵ_r used because the

dielectric causes the active region to appear nearer the apex at a given

frequency thus allowing for a reduced spacing between a resonant

element and the floor as required by the presence of the dielectric. It

is clear that use of the dielectric permits use of a cavity which is

shorter for a given lowest frequency than with a dielectric. Since the

floor angle, δ , remains constant, a shorter cavity represents an

important saving in volume. If the premittivity could be carried to an

extreme, say 100, a very compact structure would result. The practical

problems remain to be solved at $\epsilon_r > 4$.

SUGGESTIONS FOR FUTURE WORK

The following areas for future study of log-periodic antennas have evolved from the present study.

(1) Determination of the characteristics of an etched antenna mounted on the surface of the dielectric filling of the cavity.

(2) Careful measurement of phase and magnitude of current distributions in the active region of the antenna.

(3) Further study to refine the design criteria of the log-periodic antenna to permit full "frequency independent" performance when the antenna is emerged in a high permittivity dielectric material.

(4) Study of the antenna design for wide band operation over a 10:1 frequency range.

(5) Study of the means of controlling radiation patterns by antenna-cavity design.

LITERATURE CITED

Bell, R. L., C. T. Elfving, and R. E. Franks, 1960, "Near-field Measurements on a Logarithmically Periodic Antenna," IRE Transactions, vol. AP-8, pp. 559-567; November.

Brownell, Fred P., 1961, "Radiation and Impedance Characteristics of a Log-Periodic Antenna Structure Near a Conducting Surface," Unpublished M.S. Thesis, Utah State University Library, Logan, Utah.

Carrel, R. L., 1961, "The Design of Log-Periodic Dipole Antennas," IRE National Convention Record, vol. 9, pt. 1, pp. 61-75.

Clark, C. C., W. L. Jones, and A. Leigh, 1962, "A theoretical and experimental investigation of flush mounting configurations for log periodic structures," Utah State University Engineering Experiment Station Report.

DuHamel, R. H., and D. E. Isbell, 1957, "Broadband Logarithmically Periodic Antenna Structures," IRE National Convention Record, vol. 5, pt. 1, pp. 119-128.

DuHamel, R. H., and F. R. Ore, 1958, "Logarithmically Periodic Antenna Designs," IRE National Convention Record, vol. 6, pt. 1, pp. 139-151.

Dyson, J. D., 1962, "Frequency-Independent Antennas," Electronics, vol. 35, pp. 39-44; April 20.

Elfving, C. T., 1961, "Design Criteria for Log Periodic Antennas," IRE WESTCON Convention Record, vol. 5.

Isbell, D. E., 1960, "Log Periodic Dipole Arrays," IRE Transactions, vol. AP-8, pp. 260-267; May.

Schelkunoff, S. A., and H. T. Friis, 1952, "Antennas: Theory and Practice," John Wiley and Sons, Inc., New York.

Smith, P. H., 1944, "An Improved Transmission Line Calculator," Electronics, vol. 17, p. 130; January.